Dipolar interactions among magnetite nanoparticles for magnetic hyperthermia: a rate-equation approach

Dipolar interactions among magnetite nanoparticles for magnetic hyperthermia: a rate-equation approach

Gabriele Barrera,[*a] Paolo Allia,[a] and Paola Tiberto[a]

Rate equations are used to study the dynamic magnetic properties of interacting magnetite nanoparticles viewed as double well systems (DWS) submitted to a driving field in the radio-frequency range. Dipole-dipole interaction among particles is modeled by inserting an *ad-hoc* term in the energy barrier to simulate the dependence of the interaction on both interparticle distance and degree of dipole collinearity. The effective magnetic power released by an assembly of interacting nanoparticles dispersed in a diamagnetic host is shown to be a complex function of nanoparticle diameter, mean particle interdistance and frequency. Dipolar interaction markedly modifies the way a host material is heated by an assembly of embedded nanoparticles in mag-netic hyperthermia treatments. Nanoparticle fraction and strength of the interaction can dramati-cally influence amplitude and shape of the heating curves of the host material; the heating ability of interacting nanoparticles is shown to be either improved or reduced by their concentration in the host material. A frequency-dependent cut-off length of dipolar interactions is determined and explained. Particle polydispersity entailing a distribution of particle sizes brings about non-trivial effects on the heating curves in dependence of the strength of dipolar interaction.

1 Introduction

The recent years have witnessed an impressive growth of concern on magnetic nanoparticles (NPs) for use in many different areas of technology and biomedicine [1]. The research activity is developing along two main lines; the first one involves the progress in materials science and chemistry with the aim to produce nanomaterials and/or nanostructures characterized by a combination of exciting properties of potential interest in biomedicine, renewable energy technology, electronics and often characterized by a high degree of engineering at the nanoscale [2, 3, 4, 5]; a second line involves the optimization of the performance of known nanomaterials such as iron-oxide based NPs, where a large margin of improvement is still possible [4, 5]. This line of development is actively followed when magnetic NPs are considered for use in biosensing and medicine, where they provide innovative solutions for the clinical treatment of a variety of diseases [1, 6], including early diagnosis [7], accurate bioimaging [8, 9] and above all significant advances in therapeutic efficacy [9, 10, 11, 12]. Anti-tumor therapies based on, or assisted by magnetic nanoparticles are effective in overcoming the resistance of some types of malignant cells to standard treatments [13, 14]. Nanoparticles made of magnetic Fe oxides such as magnetite, maghemite or a combination of both have been long since recognized as the most promising nanomaterials for *in-vivo* applications [15, 16], owing to the ease of preparation [17] and low toxicity[18]. Fe-oxide nanoparticles in the range 10-20 nm can be used either as magnetically driven nanocarriers in standard or heat-assisted drug delivery [19, 20] or as magnetically activated, pointlike heat sources in magnetic hyperthermia [10]. The latter practice has come to play a central role in *precision nanomedicine*, an innovative branch of medicine where nanotechnology helps overcoming treatment resistance of cancer cells by exploiting the physical properties of nanomaterials [21, 22, 23]. Magnetic hyperthermia is presently being widely investigated either as a standalone therapy or in strict association with chemotherapy, enhancing its therapeutic efficiency and improving tumor penetration [24]. Anti-tumor therapies based on hyperthermia resulting from inoculated nanoparticles of magnetite have already been tested and administered to patients [25, 26].

Magnetic hyperthermia is based on heat generation by effect of cyclic magnetization of ferro- or ferrimagnetic NPs in a diamagnetic host. Heat is produced by the dynamic response of magnetic dipole moments under the action of a periodic magnetic field of suitable amplitude and frequency (usually, in the low radio-frequency range, i.e. from 20-50 kHz to about 1 MHz [27]). The main mechanisms of magnetic energy dissipation resulting in heat transferred to the host are Brown's and Néel's relaxations

[a]*INRIM, Advanced Materials Metrology and Life Sciences, Strada delle Cacce 91, I-10135 Torino, Italy. Tel: +39 011 3919858; E-mail: g.barrera@inrim.it*

† Electronic Supplementary Information (ESI) available: [file: G.Barrera et al ESI.PDF]. See DOI: 00.0000/00000000.

[28], the former effect being related to the oscillation/rotation of each nanoparticle viewed as a rigid body by effect of a magnetic force/torque, and the latter one to cyclic rotation and/or reversal of particle's magnetization with respect to the crystal axes. Néel's relaxation largely predominates at the radio frequencies of interest for magnetic hyperthermia [29] and the key physical property is the hysteresis loop of the magnetization, whose area is directly proportional to the heating power released to the neighboring tissue [22, 30]. It should be remarked that at high frequency the cyclic magnetization of NPs is hysteretic even in particles exhibiting a superparamagnetic behavior in quasi-static conditions [31, 32]. Magnetic hysteresis appears because at high frequency the particle's magnetization is constantly kept out of equilibrium by the driving field.

Rate equations are particularly appropriate to accurately model off-equilibrium properties of an assembly of magnetic nanoparticles described as classical two-level systems (DWS) [32, 33], provided that some conditions on magnetizing frequency and particle size are complied with [30]. Solving the rate equations allows one to obtain the evolution of the population in the two wells by effect of and driving field and temperature, so that the evolution of magnetization can be immediately derived [30, 34].

Although the rate equation framework is only an approximate way to study fast magnetization dynamics in nanostructures [30], it turns out to be an accurate, flexible technique [30, 23]with the great advantage of providing better physical insight than other methods of numerical simulation. Moreover, rate equations have been recently shown to effectively predict and describe new effects related to the use of unconventional driving-field waveforms [30] and to the control of the driving field during a clinical treatment, resulting in a fine tuning of the treatment temperature and a reduction of treatment time [23].

So far, rate equations have been typically applied to non-interacting nanoparticle systems [33, 35, 36, 34, 30, 32]. This is a direct consequence of their formal structure [32] which is best suited to describe independent DWS and cannot be immediately extended to study particle interactions. However, dipolar interactions among magnetic nanoparticles are not negligible in assemblies of concentrated NPs and markedly influence their heating efficiency, although the question is still open whether the effects of interaction are actually detrimental or beneficial, owing to the contrasting experimental and/or theoretical evidence gathered in favor of either conclusion. In fact, dipole-dipole interaction has been shown to enhance [37, 38, 39, 40] or reduce [41, 42, 43, 38, 44, 39] the heating efficiency of an assembly of NPs with respect to the non-interacting case. Recently, the attention has been focused on the heating capability of more complex arrangements of particles such as clusters, aggregates, hybrid structures where dipolar or contact interactions induce cooperative magnetic effects [45, 46]. Remarkably, some studies were done in *in vivo* conditions or inside living cells [47, 48].

Often, dipolar interaction among nanoparticles for magnetic hyperthermia is accounted for by introducing an *ad-hoc* term in the Fokker-Plank equation [38], or in the stochastic Landau-Lifshitz equation [42, 49, 50], or in the expression of the energy exploited in a Monte Carlo simulation [41, 43, 39, 51]. However, the outcomes of these methods often do not help clarify the role of interaction on the basis of physical considerations. Using a rate equation framework is expected not only to provide an alternative viewpoint but also to shade new light on this matter.

In the present model the effect of dipolar interaction is modeled through a suitable change of the energy barrier of the DWS.

Rate equations are solved for an assembly of magnetite nanoparticles with randomly directed easy axis directions, at different temperatures and for different values of driving field's amplitude and frequency. In this way, the time evolution of the population in the energy wells of the DWS is accurately determined, so that the hysteresis loops can be drawn and their area calculated as a function of the relevant physical parameters. The effective power released by interacting nanoparticles to a diamagnetic host material is inserted into a heat equation with appropriate boundary conditions in order to study the evolution of the temperature increment in the host as a function of both space and time.

Dipolar interactions turn out to have complex effects on the thermal efficiency of monodisperse and polydisperse magnetite nanoparticles. In particular, interacting particles are shown to be either more or less efficient than non-interacting particles, depending on the volume fraction. A frequency-dependent cut-off length of dipole-dipole interaction is predicted to exist. All results are explained on the basis of simple considerations on the redistribution of the DWS populations by effect of temperature and magnetic field.

2 Model

2.1 Rate Equations and Dipolar Interactions

Rate equations have proven to be a powerful tool in the analysis of the behavior of magnetic nanoparticles (NPs) described as classical double-well systems (DWS) [35, 52, 34, 32, 30]. The DWS model [34, 32, 22, 23] applies when the magnetic behavior of particles is dominated by a predominantly uniaxial magnetic anisotropy. The particles are assumed to be made of magnetite, which is nowadays the most promising iron oxide exploited in magnetic hyperthermia, and are characterized by volume $V = (\pi/6)D^3$ (D being the average NP diameter) and magnetic anisotropy K_0, whose value in magnetite NPs [31] is such that the quasi-static blocking temperature [32] $T_B \simeq K_0 V/25k_B$ is well below room temperature (T_0 = 300 K). In this paper, the following room temperature values of saturation magnetization and magnetic anisotropy have been used: $M_s(T_0)$ = 350 emu/cm^3 (350 kA/m) and $K_0(T_0) = 2\times10^5$ erg/cm^3 (2×10^4 J/m^3). Magnetic anisotropy may contain both volume and surface contributions [53], and is a single-particle property.

Rate equations describe the redistribution of magnetic moments in the two energy wells of a DWS (see Electronic Supplementary Information) by effect of temperature and/or magnetic field, both at equilibrium and off-equilibrium, according to the classical Arrhenius law [34]. As a consequence, magnetic hysteresis loops can be calculated at different temperatures, under different driving-field waveforms and over extended frequency intervals [32, 30, 22], provided that their limits of validity (discussed in detail elsewhere [30, 32]) are taken into account. In

particular, rate equations in magnetic NPs can be derived from the Fokker-Planck equation [54] when the energy barrier E_B is significantly larger than thermal energy k_BT; for the magnetic anisotropy values considered here, such a condition is fulfilled at all temperatures of interest when $D \gtrsim 12$ nm; as a consequence, the smallest size investigated in this paper is $D = 13$ nm. The driving field frequency f is in the range $1 \times 10^3 \leq f \leq 1 \times 10^6$ Hz, i.e., well below the upper limit of validity of the method ($\approx 1 \times 10^7$ Hz) [30].

The rate equation formalism used in this paper has been described in detail elsewhere [34, 30]; an overview can be found in the Electronic Supplementary Information.

Magnetite particles are assumed not to be in contact with each other, to be rather evenly dispersed in the host material, and not to aggregate in clusters nor order in chains. In fact, the aim of this work is to highlight the effect of dipolar interactions on the magnetic properties and heating efficiency of the NPs rather than on the consequences of the arrangement in space of the particles themselves. Although linear chains of large magnetic nanoparticles were shown to be characterized by a greater heating efficiency than evenly dispersed particles of comparable size [40, 55, 56], chains can be broken by a high-frequency driving field [57]. In addition, magnetic mesostructures can be harder to eliminate after a clinical treatment: removal of non-biodegradable particles or aggregates from the body is both a central issue and a complex process [58]; inoculated nanoparticles larger than about 5.5 nm are typically removed through the hepatobiliar path, which is much easier to take by smaller than by larger particles [58] and *a fortiori* nanoparticle aggregates and chains.

In the explored frequency range, the dominant mechanism of heat generation by magnetic NPs is Néel's relaxation, Brown's relaxation effects being negligible [29]. In *in-vivo* applications Brown's relaxation is further reduced because particles inoculated in a living body typically settle in definite positions around an organ in the body, losing to a large extent their rotational and translational degrees of freedom [59, 60].

In the rate-equation framework, a central role is played by thermally assisted redistribution of DWS populations between wells $i = 1,2$ [31, 34] (see Electronic Supplementary Information) which occurs in a characteristic time (different for $1 \to 2$ and $2 \to 1$ transitions under a magnetic field):

$$\tau_i = \tau_0 \exp\left(\frac{E_{Bi}}{k_B T}\right) \qquad (i = 1,2) \tag{1}$$

where $\tau_0 \approx 10^{-9}$ s and $E_{B1,2}(H,\phi)$ are the total energy barriers for $1 \to 2$ transitions and viceversa; when $H = 0$, $E_{B1} = E_{B2} = E_B$, so that a single characteristic time $\tau = \tau_0 \exp\left(E_B/k_BT\right)$ is defined. The energy barriers E_{Bi} also depend on the angle ϕ between the easy axis of the DWS and the magnetic field. Usually, a 3D random distribution of particles' easy axis directions is assumed, and all model's results are to be averaged over all angles [34, 32].

In the literature, the effect of dipolar interactions on the magnetic properties of NPs is described in a variety of ways, basically consisting in introducing either a dipolar field [42, 39, 61] or a dipole-dipole energy [49, 51, 38, 43] in an assembly of NPs. A simple but very effective way to include dipolar interactions in the rate-equation framework is to add a positive term to the energy barrier E_{Bi} of the non-interacting DWS. A higher energy barrier means that dipole-dipole interaction basically acts against the changes in the magnetic state of a nanoparticle system, both at equilibrium (resulting, e.g., in the increase of the quasi-static blocking temperature [62, 63]) and out of equilibrium, hindering the redistribution of population in the two wells of the DWS by effect of the periodic field and resulting in a larger magnetic hysteresis.

In fact, an enhancement of E_{Bi} with respect to the non-interacting case by effect of dipole-dipole interactions is supported by a variety of experimental results [64, 65, 53, 66] and is often assumed as a starting point in theoretical models or simulations [67, 68, 69]. The model can be assimilated to a mean-field theory and is therefore conceptually simpler and less deep-rooted than numerical simulations of dipole-dipole interaction in more fundamental equations for the magnetization dynamics [38, 42, 49, 50]. Collective magnetic states possibly arising in samples with a high particle concentration by effect of inter-particle dipole interactions, and resulting in spin-glass-like arrangements for randomly distributed particles [70], cannot be described by a mean-field theory; however, a collective behavior is typically found in NP systems whose concentration is much higher than the ones typically exploited in magnetic hyperthermia applications [70]. Moreover, as for all mean-field models, the simplicity of the approach allows one to achieve physical insight of the role of dipolar interaction on the magnetic properties and the heat released by an assembly of nanoparticles.

The total energy barrier of a DWS is viewed as composed of two terms, i.e., the energy deriving from the particle's magnetic anisotropy and a contribution accounting for the effect of dipole-dipole interaction on the DWS in an average way. The magnitude of the latter term is assumed to depend on the inverse cube of the interparticle distance and the degree of alignment of all magnetic dipole moments in the system, as suggested by the existing literature [71, 72, 73]. As a consequence of the variation with interparticle distance, the dipolar contribution explicitly depends on the volume fraction of nanoparticles. Non-interacting particles correspond to the limit of infinite interparticle distance.

In a monodisperse system comprised of particles separated by an average center-to-center distance $d > D$, the maximum r.m.s. dipolar energy can be written as:

$$E_D^{max} = \alpha \frac{\mu^2}{d^3} = \alpha M_s^2 V \frac{V}{d^3} = \alpha M_s^2 V f_V \tag{2}$$

where $\mu = M_s V = \frac{\pi}{6} M_s D^3$ is the magnetic moment of NPs in the macrospin approximation [34] and α is a dimensionless numerical constant deriving from purely geometrical considerations and obtained by summing the dipole-dipole energy contributions which derive from the magnetic moments surrounding each particle ; in this work, we take $\alpha = 10$, a value given in the literature [74]. The dependence of the energy barrier on the inverse cube of the interparticle distance was experimentally verified [75] by measuring the behavior of the blocking temperature in magnetic

iron oxide particles with properly tunable d. Note that the volume fraction of particles embedded in the host medium is univocally related to the interparticle distance by the relation $f_V = V/d^3$, so that the dipolar energy actually scales with f_V. The expression of f_V is easily obtained from the ratio of the total magnetic volume of N particles $V_{NP} = NV$ to the volume of the host medium which contains the N particles, $V_H = Nd^3$. This has remarkable consequences on the magnetic and thermal behavior of an assembly of interacting particles.

Existing theories or simulations [71, 72, 73] show that in disordered systems the magnitude of the dipolar field on each particle is largest when the magnetic moments are completely disordered and is strongly reduced (by a factor which can be of the order of one half) when moments are collinear. The effect is particularly apparent for volume fractions in the 0.1 - 0.35 range and determines a variation of the local dipolar energy with the degree of magnetic order of the system. In order to approximately take into account this effect, the dipolar energy has been modeled as:

$$E_D = \alpha M_s^2 V\,(1 - \frac{|m_0|}{2}) f_V \equiv E_D^{max}(1 - \frac{|m_0|}{2}) \qquad (3)$$

where $|m_0| = |M_0|/M_s$ is the absolute value of the reduced magnetization of a non-interacting system of monodisperse particles with randomly distributed easy axes (the dimensionless quantity $|m_0|$ takes values between 0 and 1). Therefore, the total energy barrier of the DWS of volume V with easy axis making an angle ϕ with the magnetic field becomes:

$$E_{Bi}(H.\phi) = E_{Bi}^0(H,\phi) + E_D = E_{Bi}^0(H,\phi) + \alpha M_s^2 V\,(1 - \frac{|m_0|}{2}) f_V. \quad (4)$$

where $E_{Bi}^0(H,\phi)$ is the barrier's height for the non-interacting system. In this way dipolar interaction, a genuine collective effect, is accounted for by modifying the energy barrier of each DWS, allowing one to treat the problem in the single-particle approximation, as for non-interacting particles. The loss of mathematical rigor is more than compensated by an increase of physical insight, as will become apparent in the following sections.

In general the product K_0V determines the magnitude of $E_{Bi}(H,\phi)$ at all angles and all magnetic field values (when $\phi = 0$ and $H \to 0$ the simple expression $E_B^0 = K_0V$ applies). The intrinsic temperature dependence of magnetic parameters such as M_s and K_0 is often neglected in the literature. However, it has been shown that the decrease of the magnitude of both quantities with temperature plays an important role on the heating properties of a system of nanoparticles [22]. Therefore, the temperature dependence of both magnetization and magnetic anisotropy is taken into account in the model. In particular, the magnetization is assumed to change with temperature according to the data reported elsewhere [76]. The Curie temperature of nanoparticles is taken as T_C = 856 K in agreement with available experimental data on magnetite particles[77, 78, 79]. The anisotropy constant $K_0(T)$ is assumed to follow a cubic power law appropriate for uniaxial symmetry [80]:

$$\frac{K_{eff}(T)}{K_{eff}(T_0)} = \Big[\frac{M_s(T)}{M_s(T_0)}\Big]^3 \qquad (5)$$

between room temperature (T_0) and T_C. This temperature dependence law was actually measured in magnetic nanoparticles containing Fe ions [81].

At each temperature, the rate equations give the occupancy numbers of the two wells as functions of the applied field for the subset of DWS making an angle ϕ with H. The hysteretic magnetization of the subset is easily obtained [32, 30]; the hysteresis loops for each ϕ angle are then summed up assuming a uniform distribution of easy axes.

2.2 Heating Model

The evolution of temperature in a non-magnetic sample containing a fraction f_V of magnetic NPs is studied by using a suitable heat equation with internal generation and appropriate boundary conditions. In this paper, a previously developed heating model [22, 23] is adopted. We make use of the standard Fourier equation in radial symmetry [22, 82, 83] with an internal power source and boundary conditions simulating heat loss dominated by forced convection.

Focusing on such a simple heat equation and simple sample geometry allows one to clarify the role of dipolar interaction on the thermal efficiency of an assembly of interacting particles in comparison to the non-interacting case. In principle, the predictions of the present approach can be improved by inserting the power generated by interacting nanoparticles in one of the bioheat equations more accurately modeling how heat is generated, transported and dissipated in a living body [84, 85]. However, many poorly known parameters influence magnetic hyperthermia in living bodies, including blood composition and density, non-uniform blood flow, thermal interactions between blood vessels and tissues, blood vessels significant for heat transfer in tissues, tissue-blood perfusion rate [22]. Therefore, use of bioheat equations accounting for such a large set of biological parameters may hinder understanding the effects of dipolar interactions, which is our primary aim here.

In our model, the nanoparticles act as pointlike heat sources evenly distributed in space throughout the sample, which is taken as a macroscopic sphere of radius $b = 0.01$ m filled with a homogeneous medium (e.g., a biological simulant or tissue phantom) where the particles are randomly distributed. The boundary conditions simulate heat loss by forced convection at the sample's boundary, a common condition in living bodies [84].

Advantages and limits of this thermal model, with particular reference to therapeutic use of magnetic hyperthermia, are discussed elsewhere [23]. Here, its main features are highlighted.

The temperature $T(r,t)$ at a distance $r \le b$ from the center of the sphere and at time t is found by numerically solving the Fourier equation for a medium with uniform thermal conductivity and thermal diffusivity:

$$\frac{\partial^2 T(r,t)}{\partial r^2} + \frac{2}{r}\frac{\partial T(r,t)}{\partial r} + \frac{W_{eff}(T)}{k} = \frac{1}{\alpha}\frac{\partial T(r,T)}{\partial t} \qquad (6)$$

where $T(r,t)$ is the local, instantaneous temperature inside

the sphere, $W_{eff}(T)$ is the effective heating power of evenly dispersed particles, k and α are the thermal conductivity and thermal diffusivity. Their values, $k = 0.5$ W/mK (applicable to real phantoms [86, 87]) and $\alpha = 1.4 \times 10^{-7}$ m^2/s, are taken as constants; although this approximation is not appropriate to a fine picture of real environments of interest in the therapeutic practice, it has been chosen in order to emphasize the role on heating played by the power released by magnetic NPs without introducing effects of non-magnetic origin such as the changes of the thermal properties of the medium. More precise results can be easily obtained by using space- and temperature-dependent thermal parameters.

Heat exchange at the sphere boundary occurs by convection with a flowing fluid surrounding the sample [22]. In living bodies, such a process occurs through tissue-blood perfusion [84]. The appropriate boundary condition is:

$$\frac{\partial T(r,t)}{\partial r}\Big|_b = -\frac{h}{k}T(b,t) \tag{7}$$

where h is the convective heat transfer coefficient. The value used in this work is $h = 133$ W/m^{2}K, corresponding to a blood perfusion coefficient typical of tumor tissues [88] (4×10^4 Wm^{-3}K^{-1}).

It should be remarked that effects arising from particle clustering or aggregation [45, 46, 47, 48, 89] are beyond the domain of validity of these magnetic and thermal models, which refer to particles almost evenly distributed in space. However, the spirit and aim of the present work is to assess the role of dipolar interaction from a fundamentalists' viewpoint, which is better done considering simpler, idealized systems characterized by a regular arrangement and a high homogeneity of particles in space. Nevertheless, the results presented in the following Sections may provide the framework for interpreting the high-frequency magnetic properties measured in aggregated nanoparticles [45, 47, 48].

3 Results

When the dipolar energy term is switched on, the hysteresis loop of a system of interacting particles turns out to markedly depend on the mean interparticle distance d and therefore on the volume fraction of nanoparticles $f_V = V/d^3$. Notable effects on the magnetic behavior and the heating efficiency of interacting particles are separately discussed in the following sections. In all considered cases, the vertex field is kept in the range 100 - 200 Oe, compatible with the values used in the experimental practice and compliant with the prescriptions introduced to avoid harm or major discomfort to the patients [28].

3.1 Concentration-dependent Loop Area and Effective Power

The effect of dipolar interaction on hysteresis loops is shown in panels $a-c$ of Figure 1 for a monodisperse system of 13 nm nanoparticles at $T_0 = 300$ K submitted to a harmonic magnetic field of vertex $H_V = 200$ Oe (15.915 kA/m) at the magnetizing frequency $f = 100$ kHz.

In the panels, the anhysteretic curve of the system at equilibrium is also shown for comparison; this curve corresponds to the cyclic magnetization measured in the limit of zero frequency. The black dashed line in panel d illustrates the standard behavior of the loop area A_L as a function of f_V. In general, the loop area starts from a small positive value for $f_V \to 0$ (i.e., $d \to \infty$), increases up to a maximum (the corresponding loop is shown in panel b), and finally goes to zero for large f_V values. Note that for small f_V the loop is slightly wider than, but similar in shape and slope to the equilibrium curve, whereas for high f_V (panel c), the loop is very far from the equilibrium curve and its area disappears because the strong dipolar interaction makes the overall energy barrier so high that the coercive field becomes much larger than the vertex field. The central role played by the ratio of the vertex field to the coercive field on the width of the hysteresis loop was elucidated elsewhere [32]: when the coercive field is much larger than the vertex field, magnetic hysteresis is expected to disappear.

The functional dependence of the loop's area on f_V is rather complex, neither it is simply related to the variation of typical hysteretic parameters such as the coercive field H_C and the magnetic remanence M_r, as shown in panel d (curves in color). The meaning of the two hysteretic parameters is recalled in panel b. Although both quantities vary in a similar way with f_V, their maxima occur at slightly different f_V values. The loop's area depends not only on H_C and M_r but also on the *shape* of the loop and exhibits a complex behavior, being superimposed to the $H_C(f_V)$ curve at low volume fraction and to the $M_r(f_V)$ curve around its maximum and beyond. Comparison with the corresponding equilibrium curves shows that a small loop area can arise either from a loop which is narrow because it is close to the equilibrium curve, as in panel a, or to a loop which is narrow because the dipolar interaction is so strong that the vertex field is well below the coercive field, as in panel c.

The presence of a maximum in the $A_L(f_V)$ curve is easily explained considering that the hysteresis loop is expected to be widest when the typical time of jump across the DWS barrier τ becomes roughly equal to the driving field period $1/f$ [22]:

$$\tau = \tau_0 \exp\left(\frac{E_B}{k_B T}\right) \approx \frac{1}{f}. \tag{8}$$

In the present case the overall energy barrier E_B is linearly dependent on f_V because of the presence of the dipolar energy term; for simplicity, we take the expression for τ at $H = 0$, an approximation that holds when the vertex field is sufficiently small (i.e., well below the coercive field H_C), as in the present case.

The condition expressed by Equation 8 is explained considering that when $\tau << 1/f$ the population of the DWS is very close to thermal equilibrium, so that the hysteresis loop is expected to be narrow; on the contrary, when $\tau >> 1/f$ the redistribution of magnetic moments between the energy wells is almost suppressed and a nearly anhysteretic curve (although not coincident with the equilibrium curve) again results. Only when $\tau \approx 1/f$ the ongo-

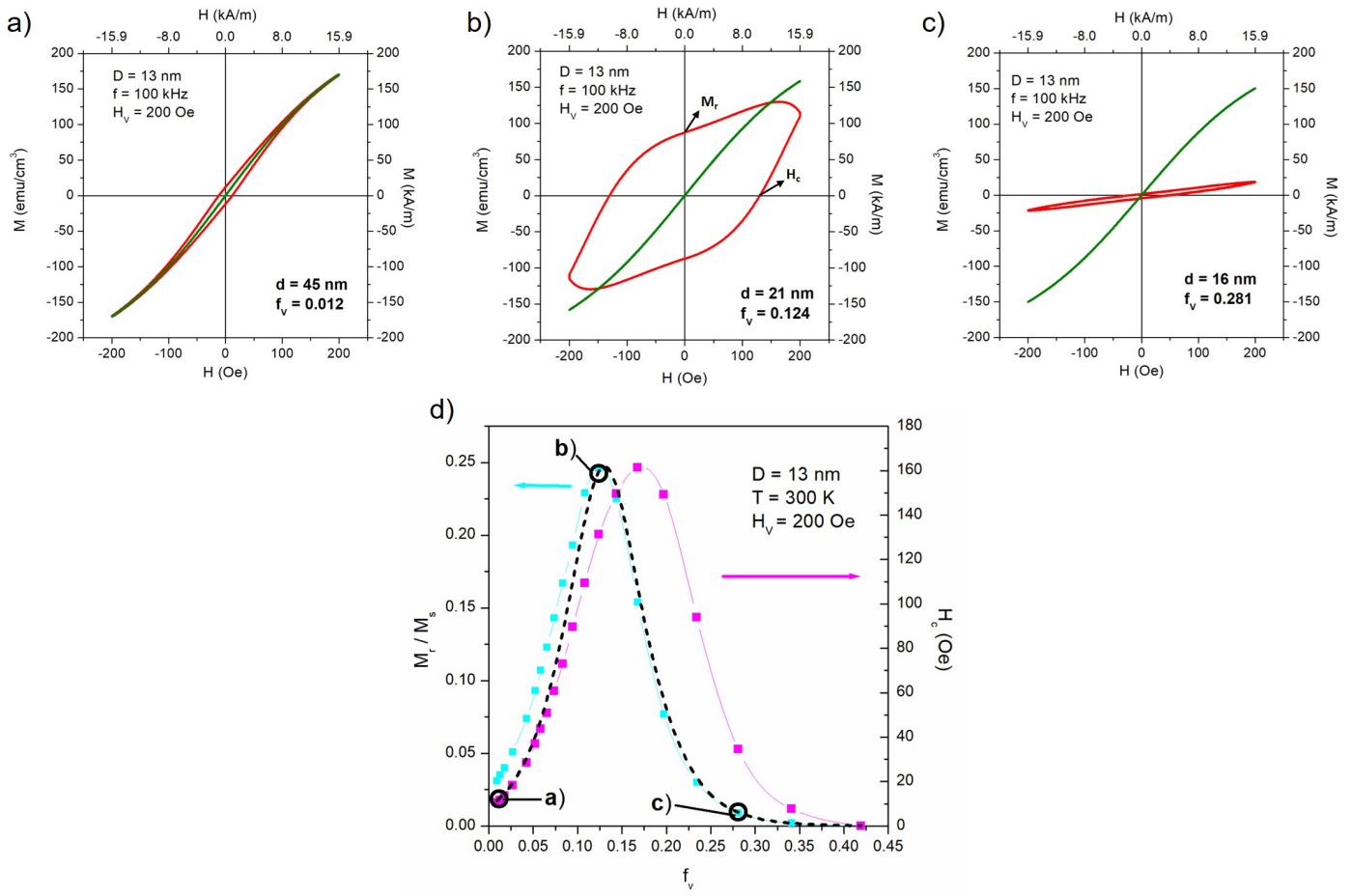

Fig. 1 Panels a - c: hysteresis loops for interacting and non-interacting particles of diameter $D = 13$ nm (red/green lines, respectively) at different interparticle distance d. The meaning of magnetic remanence M_r and coercive field H_C is recalled in panel b. Panel d: variation of the hysteretic properties (reduced magnetic remanence M_r/M_s and coercive field H_C) of interacting monodisperse particles with nanoparticle volume fraction f_V; the behavior of the loop area A_L is superimposed for comparison (dashed black line; labeled circles correspond to the loops shown in panels a - c.

ing effect of population redistribution keeps the DWS constantly out of equilibrium during a driving field's period, resulting in a particularly wide loop.

The validity of such an explanation is verified in Figure 2. In the left panel, the behavior of the room-temperature loop area A_L is reported as a function of f_V for four monodisperse systems characterized by different particle diameters and submitted to a driving field with $H_V = 100$ Oe (7.958 kA/m) and $f = 1 \times 10^5$ Hz. The $A_L(f_V)$ curves exhibit a bell-like shape, as already shown in Figure 1; the position of the maximum is displaced towards lower values of f_V with increasing the particle diameter D. In the same panel, the behavior of $\log_{10}\tau$ at room temperature and for the same diameters is also reported (oblique straight lines). The common logarithm of τ depends linearly on E_B and hence on f_V:

$$\log_{10}\tau = 0.43429 \times \left(\ln\tau_0 + \frac{E_B}{k_B T}\right) = A + B f_v. \qquad (9)$$

where $A = 0.43429 \times \ln(\tau_0 + \frac{K_0 V}{k_B T})$ and $B = 0.43429 \times \frac{\alpha}{k_B T} M_s^2 (1 - \frac{|m_0|(H=0)}{2})$ (see Equation 4).

It can be observed that the maximum of each $A_L(f_V)$ curve is always close to the value of f_V when the corresponding $\log_{10}\tau$ line crosses the horizontal line $\log_{10}(1/f) = \log_{10}(1 \times 10^{-5}) = -5$. For large particles ($D = 16$ nm) the $A_L(f_V)$ curve decreases for all values of f_V because the corresponding $\log_{10}\tau$ line does not cross the -5 line for any positive f_V.

The right panel refers to a monodisperse system of nanoparticles with $D = 13$ nm at room temperature and shows that the condition expressed by Equation 8 retains its validity over a wide range of frequencies (1 to 500 kHz): the maxima of the $A_L(f_V)$ curves always occur very close to the intersections between the $\log_{10}\tau$ line (oblique straight line) and the horizontal straight lines corresponding to the values of $\log_{10}(1/f)$). The f_V values investigated here are compatible with the requirement that no collective effects arising from dipolar interaction should be present in the system; as a matter of fact, the *strong interaction* regime where the present model is certainly not applicable can be defined by the condition $E_D^{(max)} >> K_0 V$ [90]; for instance, if one takes $E_D^{(max)} \lesssim 3 K_0 V$ as the condition for applying the model, this implies $f_V < \frac{3K_0}{\alpha M_s^2} \simeq 0.49$.

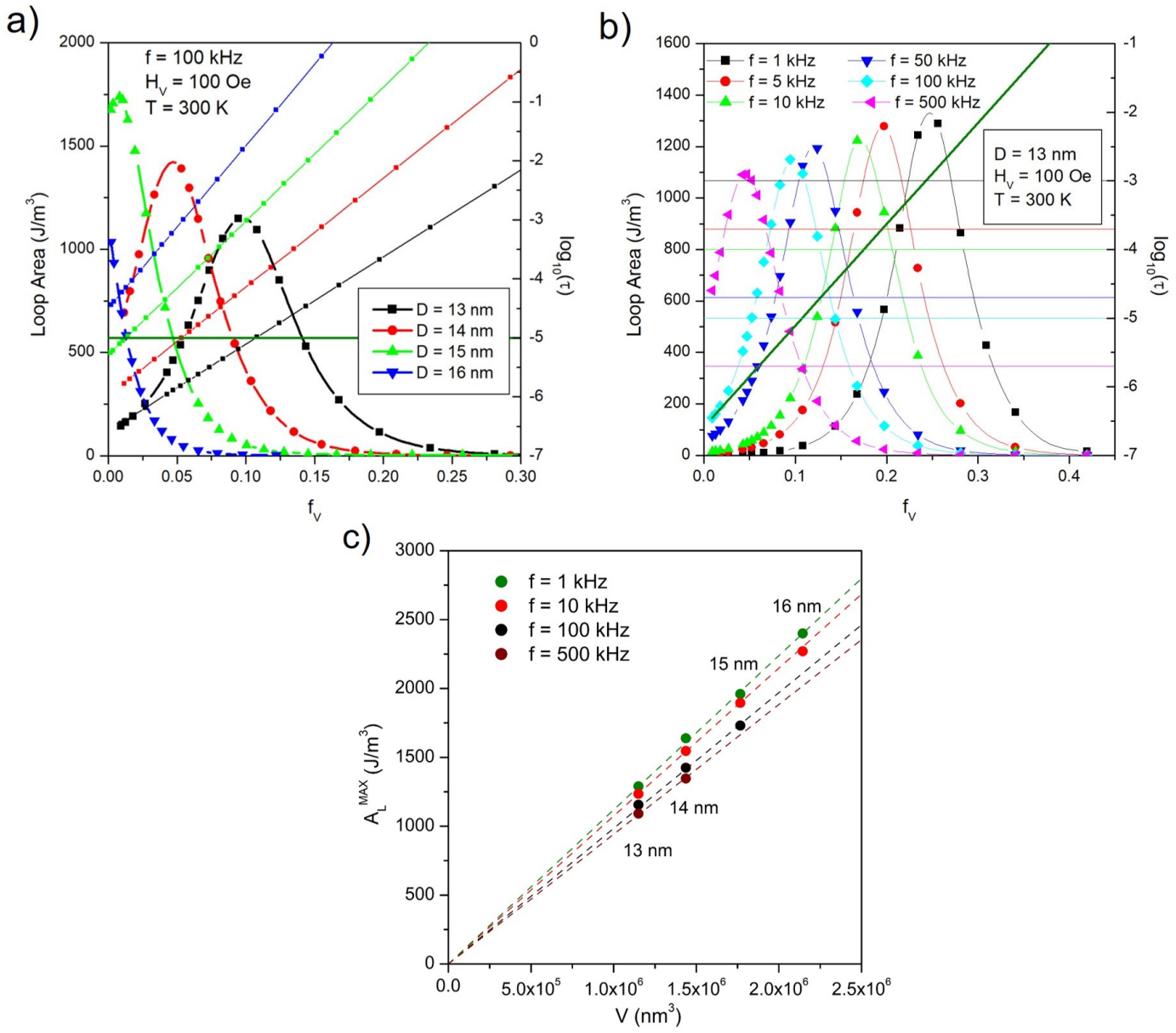

Fig. 2 Panel a: area of hysteresis loops at 100 kHz as a function of volume fraction for monodisperse systems characterized by different nanoparticle diameters (bell-like curves); oblique straight lines: behavior of the common logarithm of the typical time of jump across the barrier for the considered diameters; horizontal line: common logarithm of the inverse of magnetizing frequency. Panel b: loop area of 13 nm-particles as a function of volume fraction for different driving-field frequencies (bell-like curves); oblique straight line: behavior of the common logarithm of the typical time of jump across the barrier; horizontal lines in color: values of $\log_{10}(1/f)$ for the considered frequencies. Panel c: behavior of the maximum loop's area $A_L^{(Max)}$ as a function of the particle volume at different driving-field frequencies. The maxima of the $A_L(f_V)$ curves for $D = 16$ nm at 100 kHz and for $D = 15$ and 16 nm at 500 kHz would occur at negative values of f_V.

3.2 Properties of Maximum Loop Area

Although the bell-shaped behavior of the $A_L(f_V)$) curve cannot be represented by a simple analytical function, Eq. 8 can be used to obtain the following rule-of-thumb expression which predicts with good approximation the concentration corresponding to the maximum value A_L^{MAX} for a given particle size D at the frequency f:

$$f_V^{(Max)} = \frac{1}{\alpha M_s^2}\Big[\frac{6k_BT}{\pi D^3} ln(1/\tau_0 f) - K_0\Big]. \quad (10)$$

When the right-hand term becomes less than zero, A_L^{MAX} is at $f_V = 0$ (corresponding to the non-interacting system).

When the condition 10 is fulfilled, the evolving magnetization of the system derived from the rate equations has magnitude proportional to the volume of the particles, so that the maximum loop area, obtained plotting $M(t)$ against $H(t)$, is proportional to V at all frequencies, as shown in panel *c* of Figure 2 and discussed in the Electronic Supplementary Information, where a simple analytic explanation is given.

Note that such a peculiar behavior is only observed around $f_V = f_V^{(Max)}$, i.e., when the the loop's area is largest. This can be explained considering that in these conditions, i.e. when $\tau = 1/f$ (see Equation 8), the natural process of redistribution of the population between the two wells is triggered by the periodic modulation of the height of the total energy barrier produced by the magnetic (Zeeman) energy term $E_Z = -\mu H(t) = -M_s V H(t)$. When the typical relaxation time of the system, τ, becomes equal to the modulation's period, the redistribution process is most effectively driven: a larger V results in a stronger triggering effect and a larger magnetization $M(t)$ (i.e., a larger loop's area), as discussed in the Electronic Supplementary Information.

The variation of loop area with the volume fraction of nanoparticles has two important consequences:

a) the Specific Loss Power of interacting NPs, defined as $W_{SLP} = (f/\rho_{NP})A_L$ where ρ_{NP} is the mass density of magnetic material [29] is not a constant parameter and cannot be considered as a sort of label attached to a specific type of magnetic NPs, as often presumed [27]; instead, it is a function of how many particles are contained in the host medium; some examples of the behavior of W_{SLP} with f_V are given in the Electronic Supplementary Information for different values of H_V;

b) the power released by interacting particles evenly dispersed in a non-magnetic medium is no longer proportional to the volume fraction, as in the case of non-interacting particles.

As a consequence, an optimum volume fraction of particles exists, as illustrated in the left panel of Figure 3, where the effective power density W_{eff} released at room temperature by a fraction f_V of particles is shown for some typical nanoparticle diameters.

The effective power density is defined as:

$$W_{eff}(f_V) = f_V \times A_L(f_V)\, f \quad (11)$$

where $A_L(f_V)\, f$ is the power released by a single particle. In all cases, a maximum of $W_{eff}(f_V)$ is observed, whose position and height strongly depend on D. In particular, the maximum height of W_{eff} markedly decreases with increasing D. Although in this example the system containing the particles with $D = 13$ nm gives the best absolute heating performance, the position of the maximum is displaced to a particle concentration which would be too high in biomedical applications [25, 91, 92]. When f_V is in the range of values suitable for clinical treatments ($f_V \leq 0.02$) the effective power can be a non-monotonic function of D, as shown in the right panel of Figure 3 for two volume fractions ($f_V = 0.01$ and 0.02) under the same conditions as in the left panel. In both cases, the diameter giving the highest W_{eff} at room temperature turns out to be $D = 15$ nm.

3.3 Effects of Dipolar Interaction on Heating Curves

An example of the temperature variation resulting in a spherical sample of radius $b = 0.01$ m is shown in panel *a* of Figure 4, where the increment above room temperature $\Delta T = T - T_0$ is shown as a function of time for three values of f_V (full lines). The particles have diameter $D = 16$ nm and are submitted to a field of vertex $H_V = 100$ Oe (7.958 kA/m) and frequency $f = 1 \times 10^5$ Hz. In this case, as well as in all other cases discussed in the present paper, the temperature evolution with time is evaluated at a distance $r = b/2$ from the center of the sphere.

The presence of the dipolar term changes not only the steady-state temperature with respect to the non-interacting case (dashed lines of corresponding color), but also the time needed to reach the steady state and the shape of the $\Delta T(t)$ curves. When particles are non-interacting, the steady-state temperature is proportional to the volume fraction f_V, and is therefore largest for the smallest interparticle distance (here, $d = 25$ nm). On the contrary, when the interaction is present, the sample is virtually not heated at all for the highest particle concentration (red line, $d = 25$ nm), because the dipolar term in the energy barrier of the DWS becomes so large that the loop area is nearly zero for the reasons already explained in Section 3.2. On the other hand, the final temperatures attained by more dilute interacting nanoparticles (blue and green lines) are higher than the ones obtained when the nanoparticles do not interact.

Therefore, dipolar interactions act to either improve or reduce the heating power efficiency of an assembly of nanoparticles, depending on their average distance, i.e., their volume fraction.

For each value of f_V the shape of the $\Delta T(t)$ curves is strictly related to the evolution of the loop's area A_L and of the effective power W_{eff} with temperature, as discussed in detail elsewhere [22]. A concise analysis of this point can be found in the Electronic Supplementary Information. The heating curve corresponding to $f_V = 0.05$ and $d = 35$ nm (full green line in panel *a*) is particularly representative of the effect of the dipolar interaction term and deserves an in-depth analysis. The evolution of temperature above T_0, shown in panel *a* for both interacting and non-interacting particles is juxtaposed against the temperature behavior of the effective power released by interacting/non-interacting NPs (full/dashed lines in panel *b*, where the temperature is displayed on the vertical axis, on the same scale as in panel *a*).

It is apparent that around $T = T_0$, the power released by non-

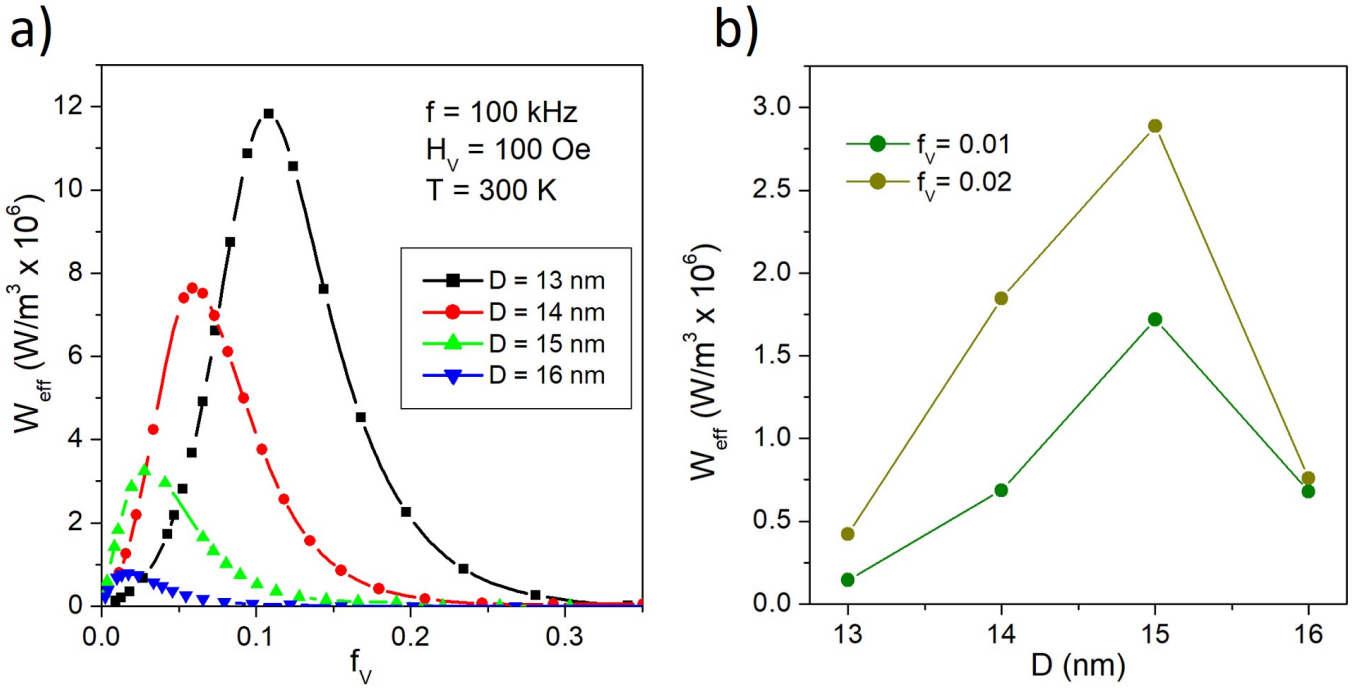

Fig. 3 Panel a: effective power released at 100 kHz as a function of particle volume fraction for different particle diameters. Panel b: effective power released at 100 kHz as a function of diameter for two volume fractions in the range used in hyperthermia applications.

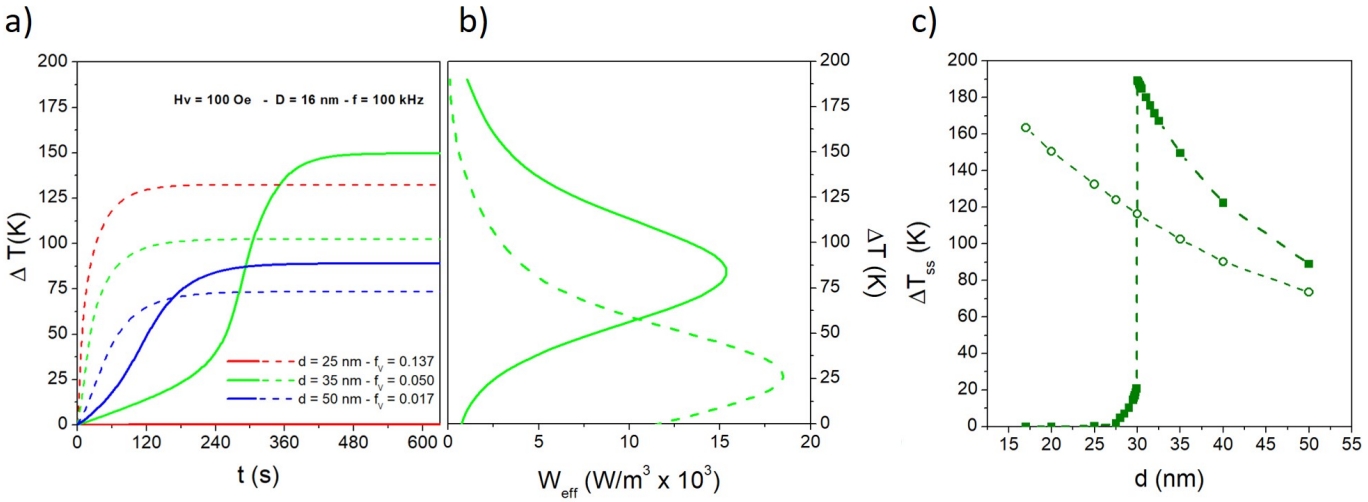

Fig. 4 Panel a: temperature increments ΔT in a sample containing monodisperse nanoparticles (D = 16 nm) as functions of time for three values of the interparticle distance (full/dashed lines: interacting/ non-interacting particles). Panel b: effective power W_{eff} and temperature increment for d = 35 nm. Panel c: effect of interparticle distance on the steady-state temperature ΔT_{SS} in a sample containing interacting / non-interacting particles (full / open symbols, respectively)

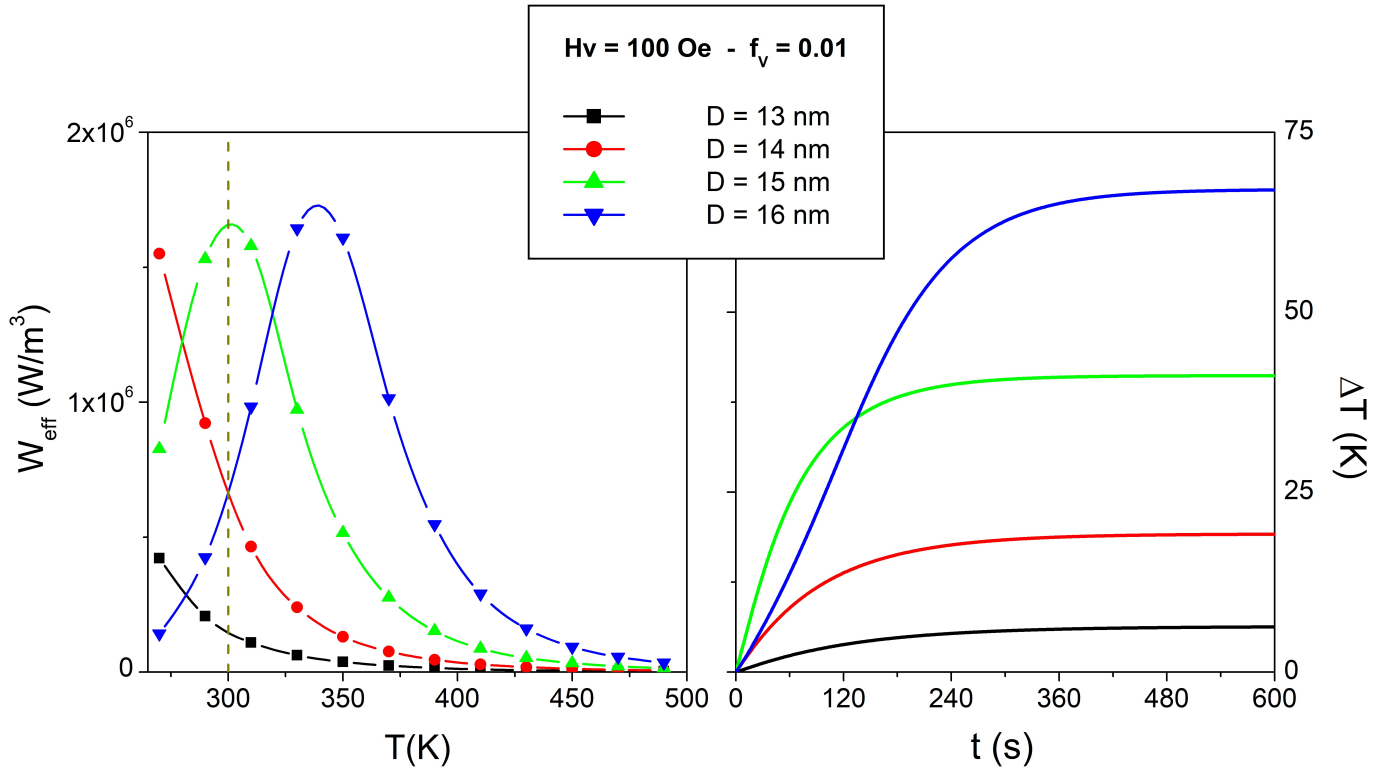

Fig. 5 Left panel: effective power as a function of temperature for different particle diameters ($f_V = 0.01$). Right panel: corresponding temperature increments as functions of time in samples containing the same volume fraction.

interacting particles is much higher than the one of the interacting system: this explains the higher initial slope of the $\Delta T(t)$ curve (dashed green line in panel a); as a consequence, the temperature where the effective power associated to the non-interacting system reaches its maximum value ($\Delta T \approx 25$ K, i.e., $T \approx 325$ K) is quickly overcome, and the subsequent reduction in W_{eff} ensures that the steady-state temperature is quickly attained by the sample.

On the contrary, the higher energy barrier E_B of the interacting system brings about a significant displacement of the whole $W_{eff}(\Delta T)$ curve towards higher temperatures (the maximum being now located at $\Delta T = 85$ K). The effective power at $T = T_0$ is now much lower than in the non-interacting case, but it is still nonzero; this gives rise to a much slower initial increase of temperature with respect to the noninteracting case; however, the effective power keeps increasing with temperature, so that the steady state is not attained before the sample enters a temperature region where the slope of the $W_{eff}(\Delta T)$ curve becomes much steeper: this circumstance is reflected in the abrupt change of slope of the $\Delta T(t)$ curve, corresponding to a much stronger heating effect; the steady state is finally reached at a higher temperature, when the maximum value of W_{eff} has been overcome. This explains both the higher final temperature and the much longer time needed to attain the steady state in the interacting case.

As a study case, the role played by dipolar interaction has been investigated in detail for monodisperse particles with $D = 16$ nm by increasing the interparticle distance in very small steps, as shown in panel c of Figure 4, where the steady-state temperature increment in the sample is reported as a function of d (full/open symbols refer to interacting/non-interacting particles, respectively). Whilst in the non-interacting case the steady-state temperature is a monotonically decreasing function, a remarkably more complex functional dependence is observed when the dipolar interaction is switched on. For sufficiently small d, the interaction is so strong that sample heating is completely inhibited, as already remarked. A very sharp transition from the no-heating to the strong heating regime is observed around a well-defined interparticle distance (in the present case, $d \simeq 30$ nm). When the strong heating regime is set up, the steady-state temperature suddenly becomes much higher than when particles do not interact. The transition is not only characterized by a discontinuity of the steady-state temperature but also by a dramatic slowing down of the time needed to reach the steady state, as further discussed in the Appendix. Finally, when d is increased above 30 nm, the temperatures attained by the sample containing interacting NPs smoothly approach from above the ones corresponding to the non-interacting case.

Similar arguments help understanding the role played by nanoparticle size on the heating efficiency of the same volume fraction of particles ($f_V = 0.01$), reported in Figure 5. The details of the heating curves reported in the right panel are explained by considering the temperature behavior of the effective power W_{eff}

shown in the left panel. For instance, the low heating efficiency of particles with $D = 13$ nm arises because of the monotonically decreasing trend of the corresponding $W_{eff}(T)$ curve; similarly, the higher slope and lower steady-state temperature of the heating curve for $D = 15$ nm (green line) with respect to the one for $D = 16$ nm (blue line) are explained by the different values of W_{eff} at $T = T_0$ (vertical dashed line in the left panel) and the different positions of the maximum of W_{eff}. The horizontal displacement of the W_{eff} curves for different particle sizes is explained by the analysis reported in the Electronic Supplementary Information.

The results highlighted in this Section help to explain why the role of dipolar interaction on the heating efficiency of magnetic NPs is still debated and many contradictory views exist. Although in many works it is concluded that dipolar interaction reduces the heating performance of nanoparticles [41, 42, 43, 38, 44, 39], in other cases dipole-dipole interaction is shown to enhance this property instead [37, 38, 39]. In fact, the existence of an optimal particle density for magnetic hyperthermia was either inferred or invoked [49, 39, 38, 61, 93, 94]. The rate equation approach and the proposed dipolar-energy model naturally explain different experimental results or views within a single framework. The model predicts that the effective power at room temperature - which controls the initial slope of the $\Delta T(t)$ curves - can be either enhanced or reduced by dipole-dipole interaction with respect to the non-interacting case, and the volume fraction f_V governs whether the dipole-dipole interaction has beneficial o detrimental effects in the heating process. On the other hand, the steady-state temperature of a sample is a quantity not only critically dependent on $W_{eff}(T)$ and therefore on f_V, but also on the details of the intrinsic temperature variation of the magnetic properties of nanoparticles.

3.4 Effective Cut-off Length of Dipolar Interaction

The existence of a finite cut-off length of dipole-dipole interaction in nanoparticle assemblies has been inferred from numerical simulations [95, 96, 43] and measurements [97, 98]. In particular, it has been suggested that the effect of interactions is quickly reduced with increasing interparticle distance and becomes almost negligible for separations exceeding about three particle diameters. These conclusions were drawn from the study of nearly-equilibrium magnetic properties, such as FC/ZFC curves, ac susceptibility and quasi-static hysteresis loops.

In the present paper dynamic, largely off–equilibrium magnetic properties are investigated, so that it becomes possible to extend the knowledge about the cut-off length to the high-frequency regime.

In the present model the non-interacting case corresponds to the limit $d \to \infty$. In fact, the shape of the loop of an interacting system becomes gradually more similar to the one of the non-interacting system when d is increased. In order to quantify this effect, the following quantity is defined:

$$\Sigma = \frac{1}{M_s}\sqrt{\sum_{i=1}^{n}\left(M_i^{(INT)} - M_i^{(N.I.)}\right)^2}, \qquad (12)$$

where the summation is extended to n selected values of the magnetization on a single closed loop, $M_i^{(INT)}$ being the magnetization of the interacting system for a given field H_i and $M_i^{(N.I.)}$ the corresponding magnetization of the non-interacting system, with $i = 1, 2, 3 \ldots n-1, n$ (in this work, n has been fixed to 1000). A graphical example of the procedure is given in the Electronic Supplementary Information. Basically, the quantity Σ can be likened to a dimensionless standard deviation having the property $\Sigma \to 0$ for $d \to \infty$. The behavior of Σ as a function of the interparticle distance normalized to the particle diameter (d/D) is reported in panel *a* of Figure 6 for a monodisperse system of interacting particles with $D = 13$ nm. It can be observed that the $\Sigma(d/D)$ curves are markedly affected by the driving-field frequency. The maximum value of Σ is found when $d \to D$ and is of the order of 5 at all frequencies.

An effective cut-off length (λ) of dipole-dipole interaction can be defined as the distance $d = \lambda$ such that $\Sigma \leq 0.1$. This condition corresponds to an almost perfect superposition of the loops of interacting and non-interacting NPs. The behavior of the ratio λ/D as a function of the driving frequency is shown in panel *b* of Figure 6. Interestingly, the cut-off length turns out to be constant and of the order of three particle diameters up to about 1×10^4 Hz, whilst for higher frequencies it increases almost linearly in the semi log graph. The low-frequency value of λ/D resulting from the present model is therefore in excellent agreement with the values emerging from the analysis of quasi-static effects [95, 96, 43, 97, 98].

3.5 Effect of Frequency on the Cut-off Length of Dipolar Interaction

The increase of the normalized cut-off length λ/D at high frequencies (panel *b* of Figure 6) can be explained through an in-depth analysis of the characteristic times involved in the rate-equation formalism.

In the time-frequency diagram sketched in the left panel of Figure 7 the two oblique straight lines represent:

- one half of the period, i.e., the time $\frac{1}{2f}$ taken by the magnetic field to reverse its sign (upper line);
- a time much shorter than the reversal time, such that the driving field can be considered as a constant; here we conventionally take one hundredth of the reversal time, i.e., $\frac{1}{200f}$ (lower line).

These lines divide the time-frequency plane in three regions depicted with different patterns and labeled as *temperature-driven* (below the $\frac{1}{200f}$ line), *field-driven* (above the $\frac{1}{2f}$ line), and *partially field-driven* (in between). The meaning of these regions is easily explained: when the spontaneous time of jump between the two energy wells is greater than $\frac{1}{2f}$, it is the applied field that drives the redistribution of the DWS population, while the temperature plays a negligible role; on the contrary, the condition $\tau < \frac{1}{200f}$ indicates that the temperature is so high that the redistribution between energy wells is much faster than the evolution of the magnetic field. Of course, the transition from one regime to the other one is not sharp, and an intermediate region exists. To be specific, let us consider the typical time of jump across the barrier ($\tau = \tau_0 \exp(E_B/k_BT)$) for an assembly of monodisperse NPs

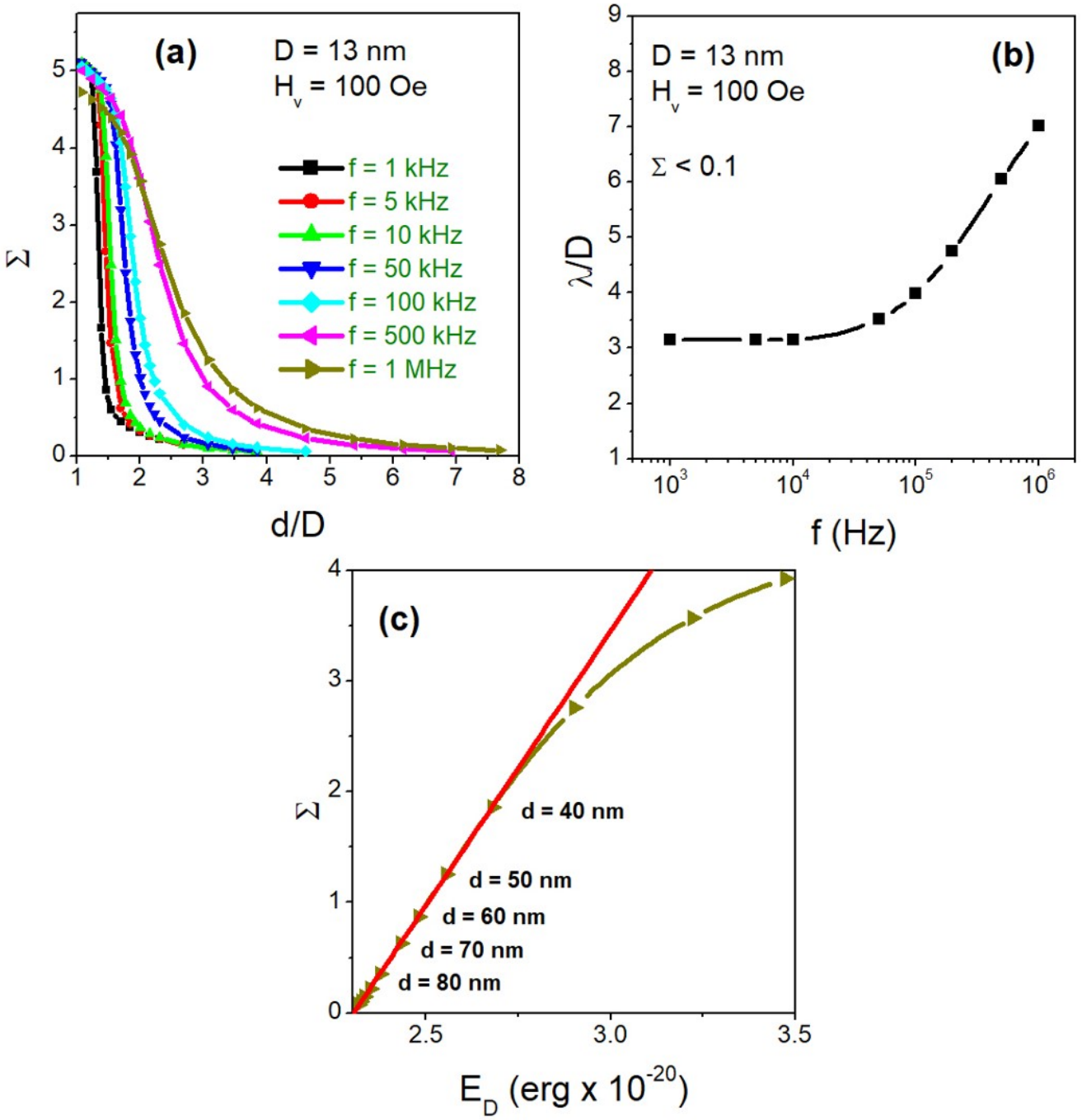

Fig. 6 Panel a: measure of the effect of interaction on the loop shape (Σ) as a function of interparticle distance normalized to the particle diameter at different magnetizing frequencies. Panel b: effective cut-off length of dipole-dipole interaction λ (normalized to the particle diameter) as a function of frequency. Panel c: proportionality between Σ and the total barrier height E_B at large interparticle distances.

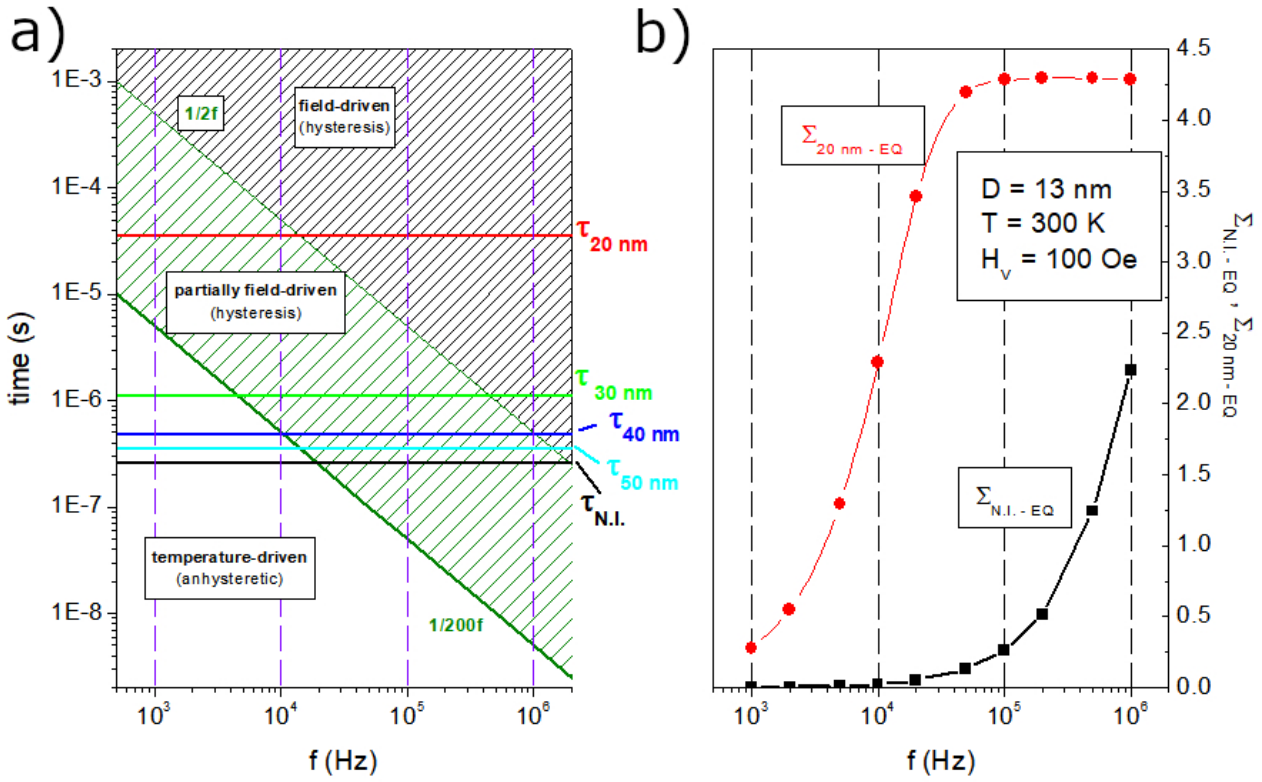

Fig. 7 Panel a: time-frequency diagram used to define the different regimes of the dynamical response of interacting and non-interacting particles to an ac driving field of fixed amplitude (see text). Panel b: effect of driving-field frequency on the difference in shape between hysteresis loops and the corresponding equilibrium curves for 13 nm-nanoparticles in non-interacting and interacting conditions (black and red curves, respectively).

at the temperature T:
- when τ falls in the temperature-driven region, the changes in the occupation numbers between the two wells are so fast that the two populations of the DWS are always equal to the equilibrium values [32]; in other words, the system is at equilibrium and the magnetization follows a Langevin-like curve with no hysteresis [34];
- on the contrary, in the field-driven region the spontaneous process of reordering is so slow that the occupancy numbers of the two wells remain virtually constant during each period, and the magnetization is modified only because of the rotation of the magnetic moments by effect of the applied field. In other words, the assembly of NPs behaves as a *blocked* system, and a large hysteresis is expected;
- in the intermediate region some change of the occupation numbers still takes places: in fact, the periodic change in barrier height triggered by the field [32] somewhat favors the population redistribution. An intermediate magnetic hysteresis is expected.

Some representative values of τ for interacting NPs with $D = 13$ nm at $T_0 = 300$ K are reported in the diagram (horizontal lines in color). The values of τ, obtained from Equation 8 for H =0, differ because of the different interparticle distance; the lowest line (in black) corresponds to the non-interacting system and is labeled $\tau_{N.I.}$. An increase of d results in a smaller energy barrier and in a lower τ-line in the diagram. For simplicity, the extreme cases only (τ_{20nm} and $\tau_{N.I.}$) will be discussed in detail.

Let us consider the non-interacting case first: at low frequencies the $\tau_{N.I.}$ line is well inside the temperature-driven region and enters the intermediate region at about $f = 2 \times 10^4$ Hz. As a consequence, the non-interacting system is predicted to be at equilibrium (anhysteretic magnetization), up to about $f = 2 \times 10^4$ Hz, while for higher frequencies the loop is expected to gradually depart from the equilibrium curve. This can be checked in the right panel of Figure 7, where the quantity $\Sigma_{N.I.-EQ}$ is plotted against frequency (black symbols). This quantity is defined by analogy with Equation 12 as:

$$\Sigma_{N.I.-EQ} = \frac{1}{M_s}\sqrt{\sum_{i=1}^{n}\left(M_i^{(N.I.)} - M_i^{(EQ)}\right)^2}, \qquad (13)$$

and measures how far the loop of the non-interacting system is from the equilibrium magnetization. As expected, the quantity $\Sigma_{N.I.-EQ}$ is exactly zero at low frequencies and begins to increase when $\tau_{N.I.}$ intersects the $\frac{1}{200f}$ line in the diagram, indicating the onset of a hysteretic behavior.

On the other hand, the τ_{20nm} line is much closer to the top of the diagram, so that it always lies inside the partially-field driven and the field-driven regions. As a consequence, one expects a nonzero hysteresis at all frequencies and an increase of the loop width when the τ_{20nm} line enters the field-driven region. This can be checked in the right panel of Figure 7, where the quantity $\Sigma_{20nm-EQ}$ (whose definition and meaning are obvious) is plotted

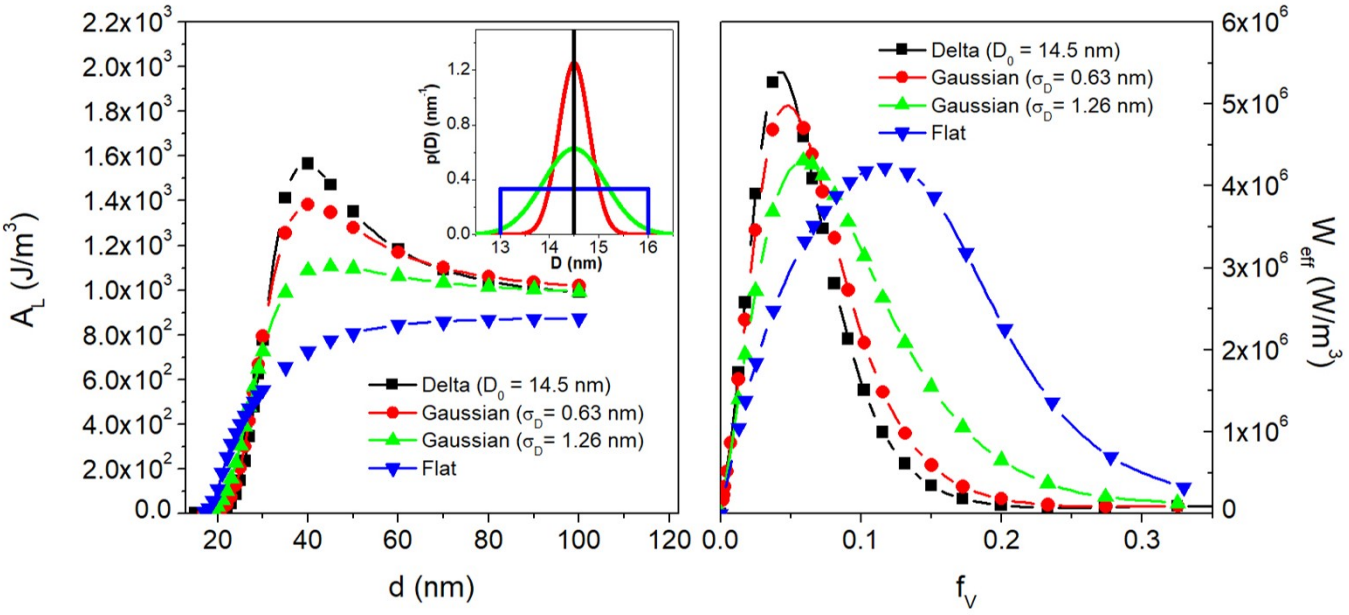

Fig. 8 Left panel: effect of interparticle distance on the loop area for polydisperse particles characterized by distribution density functions peaked at D = 14 nm; the $p(D)$ curves are shown in the inset. Right panel: effect of particle size distribution on the shape of the $W_{eff}(f_V)$ curves.

against frequency (red symbols).

The diagram of Figure 7 explains the increase observed in the normalized cut-off length λ/D above about 1×10^4 Hz, shown in panel *b* of Figure 6. Let us suppose that the interparticle distance d is continuously varied from D to infinity. At low frequencies ($f \leq 1\times10^4$ Hz), a rather small value of d (approximately, $d \geq 2D$) is sufficient to bring down the τ-line well inside the temperature-driven region; therefore the loop becomes soon coincident with the anhysteretic equilibrium curve and the quantity Σ quickly drops to zero. A small, frequency-independent value of λ/D is therefore predicted and observed (see Figure 6, panel *b*). It should be remarked that in the low frequency region the system is always at or very close to equilibrium, so that the agreement of our estimate of the λ/D ratio with the values given in the literature [95, 96, 43, 97, 98] is not unexpected.

On the contrary, in the high frequency limit ($f \geq 5\times10^5$ Hz) the system is always either inside the field-driven or the partially field-driven region; as a consequence, the loops mainly obey to the general laws ruling hysteretic effects in blocked particles. In that case, the coercive field H_C of the loop is proportional to the maximum energy barrier $E_B^{max} = E_B^0 + E_D^{max} = E_B^0 + \alpha M_s^2 V^2/d^3$ (see Equations 2 and 4). As a consequence, the hysteresis loops of an interacting system is wider than the one of the noninteracting system, while the two loops are almost the same along the vertical axis. Therefore, the difference in shape measured by the quantity Σ defined in Equation 12 is expected to be basically dominated by the difference between their coercive fields, i.e., $\Sigma \sim \left(H_C^{INT} - H_C^{N.I.}\right)$. On the other hand, the latter quantity is proportional to the difference between energy barriers, i.e., $\left(H_C^{INT} - H_C^{N.I.}\right) \sim E_D^{max} \sim d^{-3}$. It is therefore expected that $\Sigma \sim d^{-3}$ at large interparticle distances. This functional dependence is accurately verified in panel *c* of Figure 6 for $f = 100$ kHz. The different behavior of Σ on d at high frequencies brings about a larger value of the effective cut-off length λ.

3.6 Effect of Size Distribution

When polydisperse nanoparticles are exploited in magnetic hyperthermia, the distribution of sizes should be kept as narrow as possible in order not only to optimize the heat output [99, 100, 29] but also to achieve optimum clinical outcomes [101, 102, 103, 104]. The rate-equation approach can be straightforwardly extended to treat polydisperse systems. Assuming a known particle-size distribution density $p(D)$ and a random distribution in space of particles of different size, separated by a mean center-to-center distance d, the overall energy barriers E_{Bi} ($i = 1,2$) of particles of given volume V whose easy axis makes an angle ϕ with the magnetic field is now:

$$E_{Bi}(H,\phi) = E_{Bi}^0(H,\phi) + E_D = \\ = E_{Bi}^0(H,\phi) + \alpha M_s^2 \frac{\overline{V^2}}{\overline{V}}\left(1 - \frac{\overline{|m_0|}}{2}\right) f_V \tag{14}$$

where $\overline{V}$ and $\overline{V^2}$ are the average values of particle volume and of its square, and use has been done of the relation $f_V = \overline{V}/d^3$. The dipolar energy is given by Equation 2 with the substitution $\mu^2 \to \overline{\mu^2} = M_s^2\overline{V^2}$. In Equation 14, $\overline{|m_0|}$ is the absolute value of the *average* reduced magnetization of non-interacting particles with random easy axes, distributed in size according to the $p(D)$ function. The loops obtained solving the rate equations for each value of ϕ and D are first summed over ϕ and finally summed up using $p(D)$ as weight function.

Two Gaussian distributions, both centered at $D_0 = 14.5$ nm and with standard deviation $\sigma_D = 0.63$ nm and 1.26 nm have been tested, together with a box-like distribution also centered at $D = D_0$ and extending from 13 to 16 nm (whose standard deviation is $\sigma_D = \sqrt{3}/2 \approx 0.87$). The results for the monodisperse system characterized by a delta-like distribution function $p(D) \sim \delta(D - D_0)$ nm are reported for comparison. The $p(D)$ functions are drawn in the inset of the left panel of Figure 8; in all cases, the contributions from particles with diameters smaller than 13 nm or larger than 16 nm are negligible. In the same panel, the behavior of the room-temperature loop area A_L (for $H_V = 100$ Oe (7.958 kA/m), $f = 1 \times 10^5$ Hz) is reported as a function of the interparticle distance d. The loop area becomes increasingly less structured and less influenced by the interparticle distance when the width of the weight function increases.

The panel to the right shows the behavior of the effective power W_{eff} as a function of f_V in all examined cases. In size-distributed systems, the particle volume fraction is defined as $f_V = \langle V \rangle / d^3$, where $\langle V \rangle$ is the average volume of the particles. Again, the curves become broader and less structured with increasing f_V; moreover. the maximum effective power is displaced towards higher volume fractions for larger σ_D values.

The heating performance of a polydisperse nanoparticle system can be strongly influenced by the standard deviation of nanoparticle sizes. In Figure 9, the two upper frames of panel *a* show that the standard deviation of the particle distribution influences the temperature behavior of the effective power W_{eff} in markedly different ways, depending on the interparticle distance.

For large d values (such as in the left frame, where the results for $d = 50$ nm are shown) the polydispersity has no marked effects: the $W_{eff}(T)$ curves are just increasingly smoothed with increasing σ_D, while keeping the same overall behavior; as a consequence, the corresponding heating curves for all considered $p(D)$ distributions, shown in the four frames of panel *b* (dashed-dotted blue lines) are just weakly modified by the width of the distribution function.

On the contrary, when the role of dipolar interactions becomes more important, i.e., for smaller d values (as in the right frame of panel *a*, for $d = 20$ nm) a much stronger effect on the shape of the $W_{eff}(T)$ curves is observed. In particular, the value of W_{eff} at $T = T_0$ increases from nearly zero in the monodisperse case to a substantial value for the flat distribution. This has important consequences on the shape and magnitude of the corresponding heating curves, displayed in panel *b* (full red curves in the four frames). As already discussed in Section 3.3, necessary conditions for a quick, effective heating of the host medium are a high value of W_{eff} at $T = T_0$ and a non-decreasing effective power just above T_0: both conditions are simultaneously fulfilled by the Gaussian distribution with $\sigma_D = 1.26$ and by the flat distribution. Polydisperse NP systems characterized by the two largest values of σ_D values give therefore rise to a strong increase of temperature.

On the contrary, the monodisperse system is not able to effectively heat the sample, because the region of maximum W_{eff} is displaced to an exceedingly high temperature whilst the effective power at room temperature (and just above) is negligible.

As a consequence, the heating curve of polydisperse, interacting NPs can be markedly influenced by the type and width of the size distribution function. It should be explicitly remarked that when the interaction is strong enough, the highest thermal efficiency is not necessarily associated to monodisperse NPs, as usually believed, but to polydisperse particles with a proper width of the size distribution function.

Taking into account a size distribution of particles makes the model more realistic; however, other inhomogeneities related to a non-uniform distribution of particles in space exist in real systems, such as concentration fluctuations, clusters or aggregates of particles [89, 105]. The power released by nanoparticles has been experimentally found to be very sensitive to aggregation effects, because of the onset of strong interparticle interactions (either dipolar or contact) which give rise to cooperative magnetic phenomena [45, 46, 47, 48]. This important aspect should be more properly addressed having clarified the role of dipolar interaction in simpler, less interacting systems as the ones studied in the present work.

4 Conclusions

Rate equations were applied to describe the effect of dipole-dipole interaction on the hysteretic properties of magnetite NPs submitted to a cyclic radio-frequency driving field, in the typical operating conditions of magnetic hyperthermia treatments.

In a mean-field approach, the interaction was pictured by an enhancement of the energy barrier of each nanoparticle viewed as a double-well system. The relative simplicity of the method allows one to explain the results in terms of the magnetic properties of nanoparticles and of the kinetics of classical double wells.

Using rate equations not only allows one to grasp the fundamental processes governing the production of heat by evenly distributed magnetic nanoparticles, but is also instrumental to predict which values of the parameters ensure the widest loop's area and/or the highest power released to a host medium.

The power released to a host material by a set of interacting NPs with random easy axes turns out to be strongly dependent on the mean interparticle distance, i.e., on the volume fraction of particles f_V. At fixed temperature, the effective power W_{eff} turns out to be a definitely non-monotonic function of f_V, displaying a sharp maximum whose position depends on the particle diameter. Such a maximum exists because the hysteresis loop is widest when the typical time of jump across the barrier (whose height is linearly dependent on the volume fraction of interacting NPs) becomes roughly equal to the driving field's period.

The following guidelines are intended to serve as indicators of the uses of magnetite particles as pointlike heaters: if one is interested in optimizing the heating performance for laboratory uses, the best choice is to deal with high concentrations (typically, up to 30%) of small particles ($< D > \approx 13$ nm); however, if much lower concentrations are required ($\ll 1\%$, as in biomedicine), the best effect is obtained using slightly larger particles ($< D > \approx 15$ nm). Moreover, smaller ($D \lesssim 11$ nm) or larger ($D \gtrsim 18$ nm) particles evenly distributed in a medium are rather ineffective as heaters, because the areas of their *minor* loops become vanishingly small.

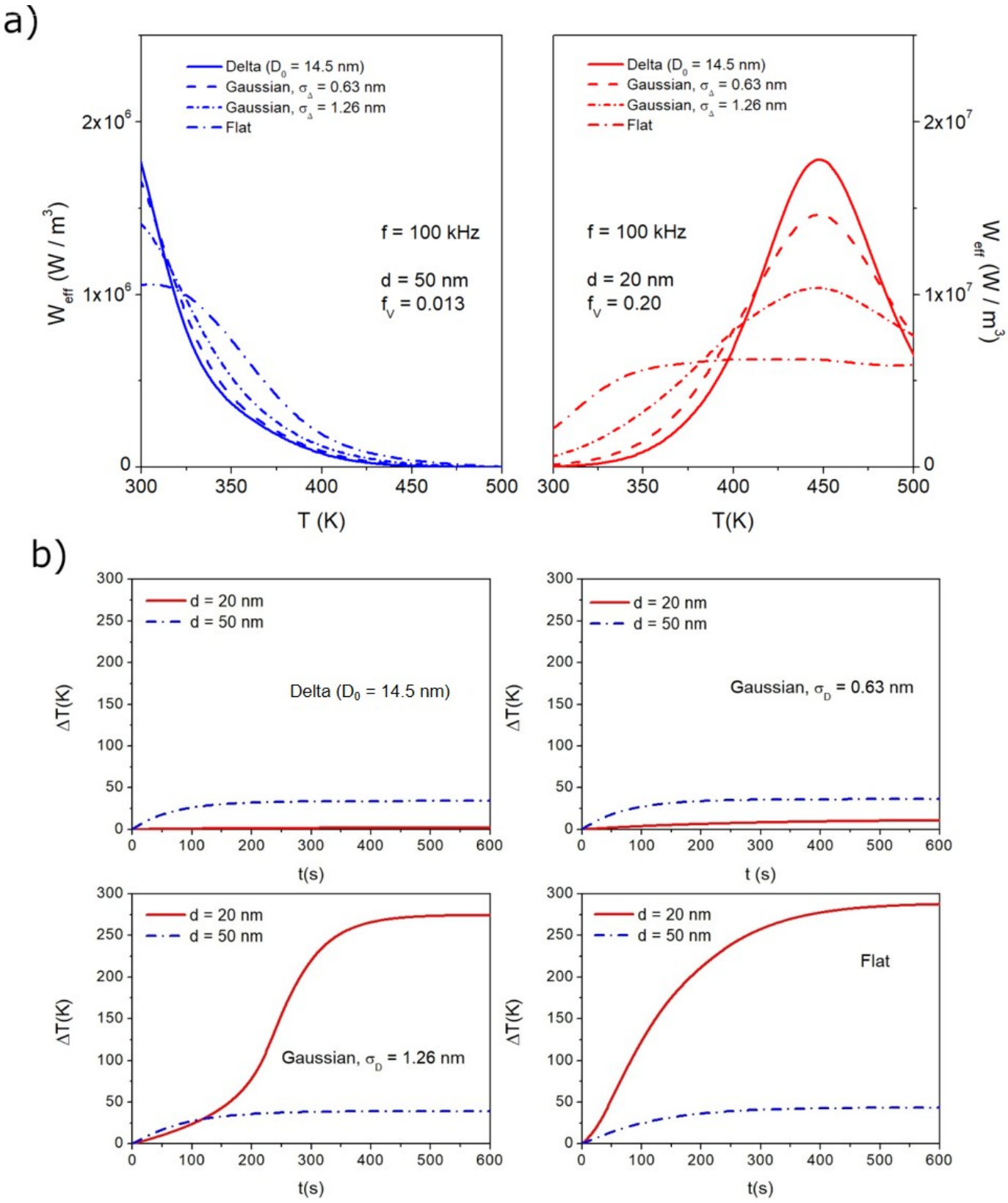

Fig. 9 Panels a: effect of particle size distribution on the $W_{eff}(T)$ curves for weakly interacting (left side) and strongly interacting (right side) particles distributed in size according to the four distribution density functions shown in the inset of Figure 8. Panels b: time evolution of the temperature increment in samples containing particles distributed in size according to the same distribution densities.

These results clearly indicate how sensitive to particle size the generated power can be.

Dipolar interaction plays a complex role on the heating process in a host material containing a fraction of almost evenly dispersed nanoparticles, resulting in temperature-time curves which can be markedly different in magnitude and shape with respect to the ones obtained in the non-interacting case.

Magnetically-induced heating of a sample containing magnetite particles was investigated by using a simple heat equation in spherical geometry, with a boundary condition mimicking the process of dissipation in living tissues where the heat generated by a distributed source is mainly removed through tissue-blood perfusion.

It was shown that an optimal particle density for magnetic hyperthermia exists, and that dipole-dipole interaction may have either a beneficial or a detrimental effect on the heating process with respect to the non-interacting case, in dependence of the volume fraction of particles. Typically, a strong dipolar interaction (corresponding to a short interparticle distance and a high f_V) hinders the dynamics of redistribution of the population between the two wells of the DWS. This results in a narrow hysteresis loop and low heating efficiency with respect to the non-interacting case. In a study case, an exceedingly sharp transition between substantially different heating regimes (no heating vs. strong heating) was shown to occur in a monodisperse system above a critical interparticle distance. Correspondingly, a dramatic slowing down of the time required by the sample to reach the steady state was observed. It should be remarked that the present approach cannot take into consideration the emergence of collective magnetic states in the system, possibly arising in highly concentrated systems, which are however expected to reduce the magnetic response and therefore the heating performance of interacting NPs more than our mean-field model can predict.

A frequency-dependent cut-off length of dipolar interactions was quantitatively determined by seeking the interparticle distance at which the shape of the hysteresis loop of interacting particles does no longer appreciably differ from the one obtained in the non-interacting case.

Below about 10 kHz the cut-off length is independent of frequency and close to the values found in the literature in quasi-static conditions ($\approx$ 3 interparticle distances), whereas above 10 kHz it steadily increases and attains a value of about 6 interparticle distances around 1 MHz. The effect is explained by considering the interplay between the driving field's half-period and the typical time of jump across the barrier. At room temperature and at low frequencies ($f \leqslant$ 10 kHz) the effect of dipolar interactions was shown to vanish much more rapidly than in the high frequency region ($f \geqslant$ 100 kHz) where the nanoparticles are continuously forced to stay away from equilibrium.

Finally, the distribution of particle sizes was investigated in polydisperse systems characterized by different distribution densities. The results were compared with the monodisperse case. The heating curves are affected, to a larger or lesser extent, by the presence of a distribution of particle sizes. In particular, for large interparticle distances (i.e., low interaction) the changes in shape and magnitude of the heating curves with respect to the monodisperse case are negligible; however, when the particles are closer to each other the changes can be much stronger and dependent on the width of the nanoparticle distribution density. Interacting particles distributed in size can heat a sample more efficiently that the same fraction of monodisperse particles.

These results have been obtained under the simplifying condition that magnetite nanoparticles are almost evenly distributed in space. Although this may be the best option in some practical applications, it is well known that in many cases, either by chance or by deliberate action, the distribution of nanoparticles is inhomogeneous in space. A non-uniform particle distribution results in a variety of magnetic and thermal properties dominated by strong interparticle interactions. The present model should therefore be regarded as a first step towards a complete understanding of the effects of dipole-dipole interaction, providing the conceptual basis for modeling more complex phenomena in inhomogeneous systems of particles.

Appendix

The study case considered in Section 3.3 helps clarify the role played by dipolar interaction and its non-trivial effects on the heating curves. In this example, monodisperse particles of diameter D = 16 nm, submitted to a driving field of frequency 100 kHz and amplitude H_V = 100 Oe (7.958 kA/m), are thought of as evenly placed in the sample at a variable interparticle distance d.

The onset of the strong heating regime is very sharp, as shown in panel c of Figure 4. In correspondence of the transition from the no-haeting to the strong heating regime, the time taken by the sample temperature to reach the steady state displays a characteristic anomaly.

The time evolution of the temperature increment in the sample (at $r = b/2$) is reported in panel a of Figure 10 for selected values of d. The steady state is assumed to be attained when the relative variation between the numerical solution of the Fourier equation at the discretized time t_i and the one at time t_{i-1}, i.e., the quantity $\Delta T/T = \Big[(T(t_i) - T(t_{i-1})\Big]/T(t_i)$ becomes less than a very small prefixed value (in the present case, less than 2×10^{-8}). This condition defines a timeout time t_{out}, which is a dramatic function of the interparticle distance; this is shown in panel a, where the lines representing the time evolution of ΔT change from full to dashed (the change marks the onset of the steady state). The slowing down of the process is particularly apparent in panel b, where t_{out} is reported as a function of the interparticle distance; the peak occurs at the distance where the switch from the two heating regimes takes place (see panel c of Figure 4).

When d is small, the heating curves shown in panel a of Figure 10 display no particular anomalies, retaining the standard shape characterized by a downward curvature. However, the timeout time grows with increasing d, indicating that the steady state is reached with even greater difficulty. In fact, the effective power released by the NPs increases with temperature by effect of the typical bell-like shape of the $W_{eff}(T)$ curve, which can be seen in

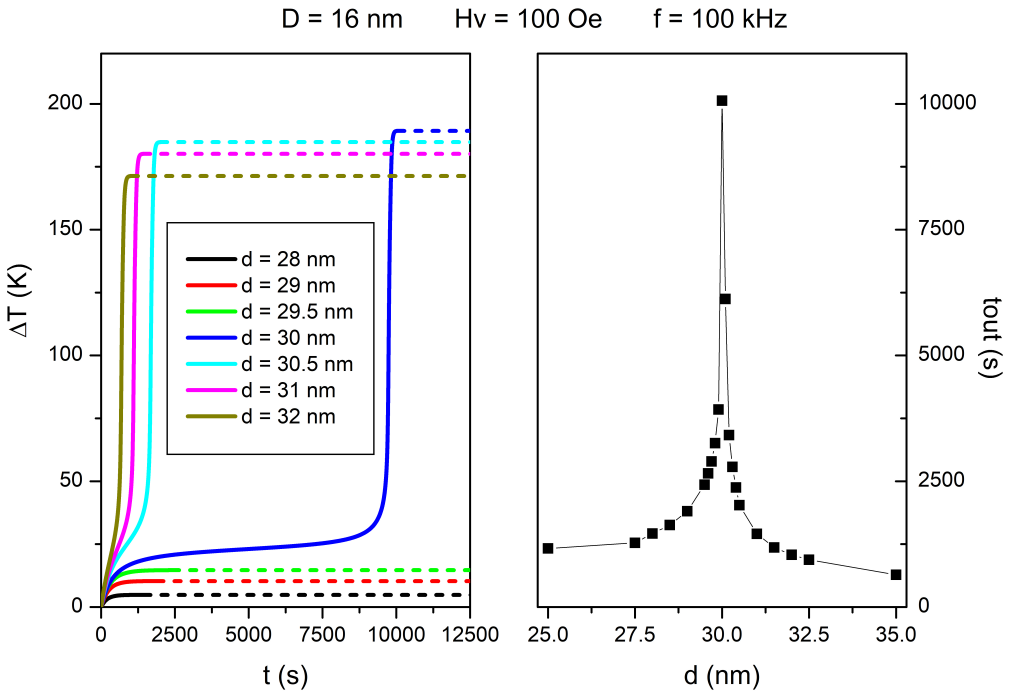

Fig. 10 Left panel: time evolution of the temperature increment for interparticle distances near to the no-heating to strong heating transition, for the parameter values reported on top of panels; the timeout time is marked on each curve by the change from full to dashed line. Right panel: timeout time as a function of interparticle distance, emphasizing the slowing-down effect for $d \simeq 30$ nm.

panel *b* of Figure 4 (full green line). As a consequence, a tradeoff between input power and losses becomes increasingly difficult to achieve.

Two quantities play a key role in determining the shape of the heating curves: the relative increment of the effective power between consecutive times $\Delta W_{eff}/W_{eff} = \left[(W_{eff}(t_i) - W_{eff}(t_{i-1})\right]/W_{eff}(t_i)$ and the relative increment of temperature $\Delta T/T$. In the left panel of Figure 11, the two quantities are plotted as functions of temperature in the interval 15-35 K (the temperature-time curve in the same interval is reported in the right panel for comparison).
$\Delta W_{eff}/W_{eff}$ is initially positive but lower than $\Delta T/T$; then the two rates become nearly coincident (and always positive, although very small). In this region the temperature keeps slowly increasing without reaching the steady state.
Above $\Delta T \approx 25$ K the quantity $\Delta W_{eff}/W_{eff})$ becomes greater than $\Delta T/T$.

In this case, a positive feedback is established (any small increment of temperature brings about a larger increase of the effective power which boosts the temperature increment), and the curvature of $\Delta T(t)$ changes of sign; the temperature keeps growing at such a high rate that an almost vertical increase is observed in the temperature vs. time graph. This anomalous behavior is observed until the peak of the $W_{eff}(T)$ curve is overcome: only there will the steady state be finally attained. Similar arguments apply to all curves calculated for $d > 30$ nm, where however the time needed by the sample to reach the region where the vertical rise of temperature occurs is significantly reduced.

Although the present example describes a very idealized case, it helps understand the complexity of effects produced by the interplay between dipole-dipole interaction and the non-monotonic behavior of the $W_{eff}(T)$ curve.

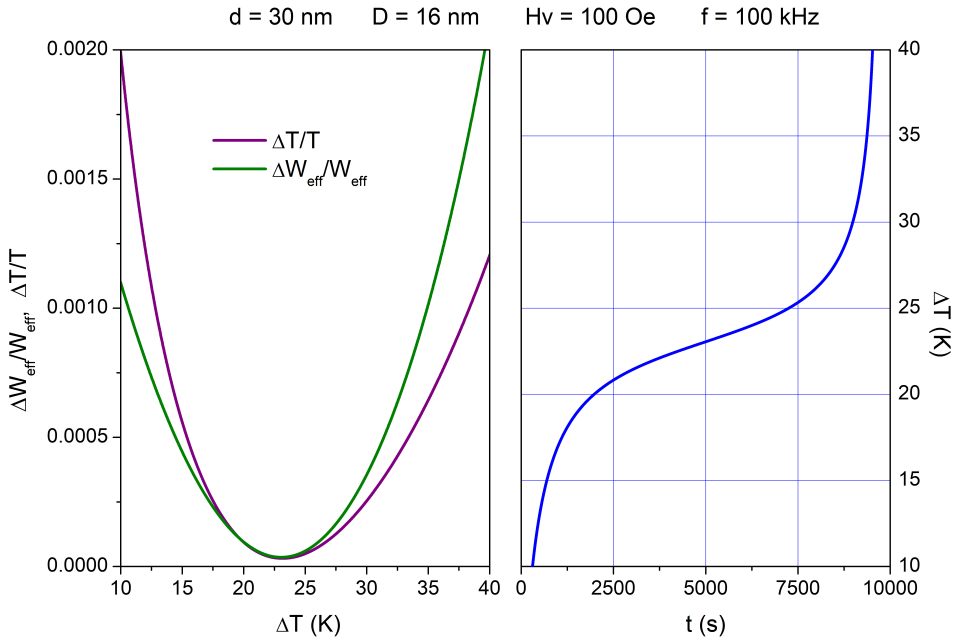

Fig. 11 Left panel: behavior of elative increments $\Delta W_{eff}/W_{eff}$, $\Delta T/T$ with temperature (see text) in the 10-40 K interval for the parameter values reported on top of the panels. Right panel: $\Delta T(t)$ curve in the same temperature interval.

Notes and references

1 K. Zhu, Y. Ju, J. Xu, Z. Yang, S. Gao, Y. Hou,*Acc. Chem. Res.*, 2018, **51**, 404-413.

2 C. Yang, L. Jia, S. Wang, C. Gao, D. Shi, Y. Hou, S. Gao, *Sci. Rep.*, 2013, **3**, 3542.

3 F. Liu, Y. Hou,S. Gao, *Chem. Soc. Rev.*, 2014, **43**, 8098-8113.

4 Z. Yang, T. Zhao, X. Huang, X. Chu, T. Tang, Y. Ju, Q. Wang,Y. Hou, S. Gao, *Chem. Sci.*, 2017, **8**, 473-481.

5 H. Zhang, Z. Yang, Y. Ju, X. Chu, Y. Ding, X. Huang, K. Zhu, T. Tang, X. Su, Y. Hou, *Adv. Sci.*, 2018, **5**, 1800271.

6 N. T. K. Thanh, *Clinical Applications of Magnetic Nanoparticles: From Fabrication to Clinical Applications*, CRC Press, 2018.

7 S. M. Dadfar, K. Roemhild, N. I. Drude, S. von Stillfried, R. Knüchel, F. Kiessling, T. Lammers, *Adv. Drug Deliv. Rev.*, 2019, **138**, 302–325.

8 A. Bakenecker, M. Ahlborg, C. Debbeler, C. Kaethner, K. Lüdtke-Buzug, *Magnetic Particle Imaging*, Elsevier Inc., 2018.

9 E. Polo, P. del Pino, A. Pardo, P. Taboada and B. Pelaz, in Nanooncology Engineering Nanomaterials for Cancer Therapy and Diagnosis, eds. G. Gonçalves, G. Tobias, Springer, Cham, 2018, pp. 239–279.

10 S. Ahmed, B. L. Rajak, M. Gogoi and H. D. Sarma, *Magnetic nanoparticles mediated cancer hyperthermia*, INC, 2020.

11 L. Zhu, Z. Zhou, H. Mao, L. Yang, *Nanomedicine*, 2017, **12**, 73–87.

12 M-K. Kim, J. Sim, J-H. Lee, M. Kim, S-K. Kim, *Phys. Rev. Appl.*, 2018, **9**, 054037.

13 S. Spirou, M. Basini, A. Lascialfari, C. Sangregorio, C. Innocenti, *Nanomaterials*, 2018, **8**, 401.

14 A. L. B. Seynhaeve, M. Amin, D. Haemmerich, G. C. van Rhoon, T. L. M. ten Hagen, *Adv. Drug Deliv. Rev.*, DOI:10.1016/j.addr.2020.02.004.

15 M. Mahmoudi, S. Laurent, *Iron Oxide Nanoparticles for Biomedical Applications*, Elsevier Ltd, 2018.

16 G. Zoppellaro, in *Magnetic Nanoheterostructures Diagnostic, Imaging and Treatment*, eds. K. S. Sharma and Y. Javed, Springer, Cham, 2020, pp. 57–102.

17 W. Wu, C. Z. Jiang, V. A. L. Roy, *Nanoscale*, 2016, **8**, 19421–19474.

18 L. S. Arias, J. P. Pessan, A. P. M. Vieira, T. M. T. De Lima, A. C. B. Delbem, D. R. Monteiro, *Antibiotics*, DOI:10.3390/antibiotics7020046.

19 B. T. Mai, S. Fernandes, P. B. Balakrishnan, T. Pellegrino, *Acc. Chem. Res.*, 2018, **51**, 999–1013.

20 I. Ortiz de Solorzano, T. Alejo, M. Abad, C. Bueno-Alejo, G. Mendoza, V. Andreu, S. Irusta, V. Sebastian, M. Arruebo, *J. Colloid Interface Sci.*, 2019, **533**, 171–181.

21 M. Hu, X. Ai, Z. Wang, Z. Zhang, H. Cheong, W. Zhang, J. Lin, J. Li, H. Yang, B. Xing, *Nano Res.*, 2018, **11**, 5474–5498.

22 G. Barrera, P. Allia, P. Tiberto, *Nanoscale*, 2020, **12**, 6360–6377.

23 G. Barrera, P. Allia, P. Tiberto, *Nanoscale Adv.*, DOI:10.1039/d0na00358a.

24 J. Ding, J. Chen, L. Gao, Z. Jiang, Y. Zhang, M. Li, Q. Xiao, S. S. Lee, X. Chen, *Nano Today*, DOI:10.1016/j.nantod.2019.100800.

25 K. Maier-Hauff, F. Ulrich, D. Nestler, H. Niehoff, P. Wust, B. Thiesen, H. Orawa, V. Budach, A. Jordan, *J. Neurooncol.*, 2011, **103**, 317–324.

26 N. D. Thorat, S. A. M. Tofail, B. Von Rechenberg, H. Townley, G. Brennan, C. Silien, H. M. Yadav, T. Steffen, J. Bauer, *Appl. Phys. Rev.*, DOI:10.1063/1.5049467.

27 L. Beola, L. Gutiérrez, V. Grazú, L. Asín, in *Nanomaterials for Magnetic and Optical Hyperthermia Applications*, eds. R. M. Fratila and J. M. De La Fuente, Elsevier Ltd, 2019, pp. 317–337.

28 S. Dutz, R. Hergt, *Int. J. Hyperth.*, 2013, **29**, 790–800.

29 S. Dutz, R. Hergt, *Nanotechnology*, 2014, **25**, 1–28.

30 P. Allia, G. Barrera, P. Tiberto, *Phys. Rev. Appl.*, 2019, **12**, 034041.

31 C. Binns, *Nanomagnetism: Fundamentals and Applications*, Elsevier, Oxford, 2014.

32 P. Allia, G. Barrera, P. Tiberto, *J. Magn. Magn. Mater*, DOI:10.1016/j.jmmm.2019.165927.

33 N. A. Usov, *J. Appl. Phys.*, DOI:10.1063/1.3445879.

34 P. Allia, G. Barrera and P. Tiberto, *Phys. Rev. B*, 2018, *98*, 134423.

35 N. A. Usov, *J. Appl. Phys.*, DOI:10.1063/1.3536632.

36 N. A. Usov, E. M. Gubanova, Z. H. Wei, *J. Phys. Conf. Ser.*, DOI:10.1088/1742-6596/1439/1/012044.

37 M. Jeun, S. Bae, A. Tomitaka, Y. Takemura, K. H. Park, S. H. Paek, K. W. Chung, *Appl. Phys. Lett.*, 2009, **95**, 1–4.

38 G. T. Landi, *Phys. Rev. B - Condens. Matter Mater. Phys.*, 2014, **89**, 1–6.

39 S. Ruta, R. Chantrell, O. Hovorka, *Sci. Rep.*, 2015, **5**, 1–7.

40 D. P. Valdés, E. Lima Jr., R. D. Zysler, E. De Biasi, *Phys. Rev. Applied*, 2020, **14**, 014023.

41 D. Serantes, D. Baldomir, C. Martinez-Boubeta, K. Simeonidis, M. Angelakeris, E. Natividad, M. Castro, A. Mediano, D. X. Chen, A. Sanchez, L. I. Balcells, B. Martínez, *J. Appl. Phys.*, DOI:10.1063/1.3488881.

42 B. Mehdaoui, R. P. Tan, A. Meffre, J. Carrey, S. Lachaize, B. Chaudret, M. Respaud, *Phys. Rev. B - Condens. Matter Mater. Phys.*, 2013, **87**, 1–10.

43 M. Woińska, J. Szczytko, A. Majhofer, J. Gosk, K. Dziatkowski, A. Twardowski, *Phys. Rev. B - Condens. Matter Mater. Phys.*, 2013, **88**, 1.

44 M. E. Sadat, R. Patel, J. Sookoor, S. L. Bud'Ko, R. C. Ewing, J. Zhang, H. Xu, Y. Wang, G. M. Pauletti, D. B. Mast, D. Shi, *Mater. Sci. Eng. C*, 2014, **42**, 52–63.

45 J. G. Ovejero, D. Cabrera, J. Carrey, T. Valdivielso, G. Salas, F. J. Teran, *Phys.Chem.Chem.Phys.*, 2016, **18**, 10594-105963.

46 D. Niculaes, A. Lak, G. C. Anyfantis, S. Marras, O. Laslett, S. K. Avugadda, M. Cassani, D. Serantes, O. Hovorka, R. Chantrell, T. Pellegrino, *ACS Nano*, 2017, **11**, 12121-12133.

47 D. H. Ortgies, L. de la Cueva, B. del Rosal, F. Sanz-Rodríguez, N. Fernández, M. C. Iglesias-de la Cruz, G. Salas, D. Cabrera, F. J. Teran, D. Jaque, E. Martín Rodríguez, *ACS Applied Mater. Interf.*, 2016, **8**, 1406-1414.

48 D. Cabrera, A. Coene, J. Leliaert, E. J. Artés-Ibáñez, L. Dupré, N. D. Telling, F. J. Teran, *ACS Nano*, 2018, **12**, 2741-2752.

49 C. Haase, U. Nowak, *Phys. Rev. B - Condens. Matter Mater. Phys.*, 2012, **85**, 2–6.

50 N. A. Usov and O. N. Serebryakova, *Sci. Rep.*, 2020, 10, 1–14.

51 I. Conde-Leborán, D. Serantes, D. Baldomir, *J. Magn. Magn. Mater.*, 2015, **380**, 321–324.

52 J. Carrey, B. Mehdaoui, M. Respaud, *J. Appl. Phys.*, 2011, **109**, 083921.

53 S. Bedanta, W. Kleemann, *J. Phys. D. Appl. Phys.*, 2009, **42**, 013001.

54 W. F. Brown, *Phys. Rev.*, 1963, **130**, 1677–1686.

55 D. Serantes, K. Simeonidis, M. Angelakeris, O. Chubykalo-Fesenko, M. Marciello, M. Del Puerto Morales, D. Baldomir, C. Martinez-Boubeta, *J. Phys. Chem. C*, 2014, **118**, 5927–5934.

56 E. Myrovali, N. Maniotis, A. Makridis, A. Terzopoulou, V. Ntomprougkidis, K. Simeonidis, D. Sakellari, O. Kalogirou, T. Samaras, R. Salikhov, M. Spasova, M. Farle, U. Wiedwald, M. Angelakeris, *Sci. Rep.*, 2016, **6**, 38382.

57 K. Simeonidis, M. P. Morales, M. Marciello, M. Angelakeris, P. De La Presa, A. Lazaro-Carrillo, A. Tabero, A. Villanueva, O. Chubykalo-Fesenko, D. Serantes, *Sci. Rep.*, 2016, **6**, 37934.

58 W. Poon, Y. N. Zhang, B. Ouyang, B. R. Kingston, J. L. Y. Wu, S. Wilhelm, W. C. W. Chan, *ACS Nano*, 2019, **13**, 5785–5798.

59 R. Di Corato, A. Espinosa, L. Lartigue, M. Tharaud, S. Chat, T. Pellegrino, C. Ménager, F. Gazeau, C. Wilhelm, *Biomaterials*, 2014, **35**, 6400–6411.

60 D. Soukup, S. Moise, E. Céspedes, J. Dobson, N. D. Telling, *ACS Nano*, 2015,**9**, 231–240.

61 M. Osaci, M. Cacciola, *IOP Conf. Ser. Mater. Sci. Eng.*, 2017, **163**, 012008.

62 J. M. Vargas, W. C. Nunes, L. M. Socolovsky, M. Knobel, D. Zanchet, *Phys. Rev. B - Condens. Matter Mater. Phys.*, 2005, **72**, 2–7.

63 V. Russier, *J. Magn. Magn. Mater.*, 2016, **409**, 50–55.

64 F. Luis, J. M. Torres, L. M. García, J. Bartolomé, J. Stankiewicz, F. Petroff, F. Fettar, J. L. Maurice, A. Vaurès, *Phys. Rev. B - Condens. Matter Mater. Phys.*, 2002, **65**, 1-10.

65 G. F. Goya, F. C. Fonseca, R. F. Jardim, R. Muccillo, N. L. V. Carreño, E. Longo, E. R. Leite, *J. Appl. Phys.*, 2003, **93**, 6531–6533.

66 S.H. Masunaga, R.F. Jardim, R.S. Freitas, J. Rivas, *Appl. Phys. Letters*, 2011, **98** 013110.

67 S. Shtrikman, E. P. Wohlfarth, *Phys. Lett.*, 1981, **85A**, 467–470.

68 J. L. Dormann, D. Fiorani, E. Tronc, *J. Magn. Magn. Mater.*, 1999, **202**, 251–267.

69 G. T. Landi, *J. Appl. Phys.*, 2013, **113**, 163908.

70 S. Morup, M.F. Hansen, C. Frandsen, *Beilstein J. Nanotechnol.*, 2010, **1**, 182-190 .

71 D. Berkov, *Phys. Rev. B - Condens. Matter Mater. Phys.*, 1996, **53**, 731-734.

72 R. Egli, *J. Geophys. Res. Solid Earth*, 2006, **111**, 1–18.

73 C. Moya, Ó. Iglesias, X. Batlle, A. Labarta, *J. Phys. Chem. C*, 2015, **119**, 24142–24148.

74 S. Morup, *Europhys. Lett.*, 1994, **28**, 671–676.

75 S. Fleutot, G. L. Nealon, M. Pauly, B. P. Pichon, C. Leuvrey, M. Drillon, J. L. Gallani, D. Guillon, B. Donnio, S. Begin-Colyn, **Nanoscale**, 2013, **5**, 1507-1516.

76 D. J. Dunlop, in *Rock Magnetism*, Cambridge University Press, 1997.

77 D. O. Smith, *Phys. Rev.*, 1956, **102**, 959–963.

78 D. J. Dunlop, *J. Geophys. Res.*, 1973, **78**, 1780-1793.

79 J. Wang, W. Wu, F. Zhao, G. M. Zhao, *Appl. Phys. Lett.*, 2011, **98**, 1-4.

80 B. D. Cullity and C. D. Graham, *Introduction to Magnetic Materials*, 2009.

81 J. Wang, H. Duan, X. Lin, V. Aguilar, A. Mosqueda, G. M. Zhao, *J. Appl. Phys.*, 2012, **112**, 103905.

82 M. Ebrahimi, *J. Magn. Magn. Mater.*, 2016, **416**, 134-140.

83 Y. Tang, R. C. C. Flesch, T. Jin, *J. Appl. Phys.*, 2017, **122**, 034702.

84 H. W. Huang, T. L. Horng, in Heat Transfer and Fluid Flow in Biological Processes, eds. B. S.M. and A. V. Kuznetsov, Elsevier Inc., 2015, pp. 1–42.

85 I. Raouf, S. Khalid, A. Khan, J. Lee, H. S. Kim, M. H. Kim, *J. Therm. Biol.*, 2020, **91**, 102644.

86 Y. Yuan, C. Wyatt, P. Maccarini, P. Stauffer, O. Craciunescu, J. Macfall, M. Dewhirst, S. K. Das, *Phys. Med. Biol.*, 2010, **57**, 2021-2037.

87 R. A. O. Jaime, R. L. Q. Basto, B. Lamien, H. R. B. Orlande, S. Eibner, and O. Fudym, *Procedia Eng.*, 2013, **59**, 30-36.

88 E. Y. K. Ng N. M. Sudharsan, *BMC Cancer*, 2004, **4**:17, 1-6.

89 L. Gutiérrez, L. de la Cueva, M. Moros, E. Mazarío, S. de Bernardo, J. M. de la Fuente, M. P. Morales, G. Salas, *Nanotechnology*, 2019, **30**, 112001.

90 D. Fiorani and D. Peddis, *Journal of Physics: Conference Series*, 2006, **521**, 012006.

91 R. Hu, S. Ma, H. Li, X. Ke, G. Wang, D. Wei, W. Wang, *Oncol. Lett.*, 2011, **2**, 1161-1164.

92 T. R. Oliveira, P. R. Stauffer, C. T. Lee, C. D. Landon, W. Etienne, K. A. Ashcraft, K. L. McNerny, A. Mashal, J. Nouls, P. F. MacCarini, W. F. Beyer, B. Inman, M. W. Dewhirst, *Int. J. Hyperth.*, 2013, **29**, 835-844.

93 C. Martinez-Boubeta, K. Simeonidis, D. Serantes, I. Conde-Leborán, I. Kazakis, G. Stefanou, L. Peã, R. Galceran, L. Balcells, C. Monty, D. Baldomir, M. Mitrakas, and M. Angelakeris, *Adv. Funct. Mater.*, 2012, **22**, 3737-3744.

94 D. F. Coral, P. Mendoza Zélis, M. Marciello, M. D. P. Morales, A. Craievich, F. H. Sánchez, M. B. Fernández Van Raap, *Langmuir*, 2016, **32**, 1201-1213.

95 J. Andersson, C. Djurberg, T. Jonsson, P. Svedlindh, P. Nordblad, *Phys. Rev. B - Condens. Matter Mater. Phys.*, 1997, **56**, 13983-13988.

96 R. W. Chantrell, N. Walmsley, J. Gore, M. Maylin, *Phys. Rev. B - Condens. Matter Mater. Phys.*, 2001, **63**, 1-14.

97 P. C. Rivas Rojas, P. Tancredi, O. Moscoso Londoño, M. Knobel, L. M. Socolovsky, *J. Magn. Magn. Mater.*, 2018, **451**, 688-696.

98 A. Cuchillo, P. Rivas-Rojas, P. Tancredi, L. M. Socolovsky, P. Vargas, *J. Magn. Magn. Mater.*, 2020, **508**, 166842.

99 R. E. Rosenweig, *J. Magn. Magn. Mater.*, 2002, **252**, 370-372.

100 A. P. Khandhar, R. M. Ferguson, K. M. Krishnan, *J. Appl. Phys.*, 2011, **109**, 2011-2014.

101 S. Sun, H. Zeng, *J. Am. Chem. Soc.*, 2002, **124**, 8204-8205.

102 L. Chang, X. L. Liu, D. Di Fan, Y. Q. Miao, H. Zhang, H. P. Ma, Q. Y. Liu, P. Ma, W. M. Xue, Y. E. Luo, H. M. Fan, *Int. J. Nanomedicine*, 2016, **11**, 1175-1185.

103 W. Xie, Z. Guo, F. Gao, Q. Gao, D. Wang, B. S. Liaw, Q. Cai, X. Sun, X. Wang, L. Zhao, *Theranostics*, 2018, **8**, 3284-3307.

104 M. Danaei, M. Dehghankhold, S. Ataei, F. Hasanzadeh Davarani, R. Javanmard, A. Dokhani, S. Khorasani, M. R. Mozafari, *Pharmaceutics*, 2018, **10**, 1-17.

105 J. Wells, O. Kazakova, O. Posth, U. Steinhoff, S. Petronis, L. K. Bogart, P. Southern, Q. Pankhurst, C. Johansson, *J. Phys. D: Appl. Phys.*, 2017, **50**, 3383003.